



저작자표시-비영리-변경금지 2.0 대한민국

이용자는 아래의 조건을 따르는 경우에 한하여 자유롭게

- 이 저작물을 복제, 배포, 전송, 전시, 공연 및 방송할 수 있습니다.

다음과 같은 조건을 따라야 합니다:



저작자표시. 귀하는 원저작자를 표시하여야 합니다.



비영리. 귀하는 이 저작물을 영리 목적으로 이용할 수 없습니다.



변경금지. 귀하는 이 저작물을 개작, 변형 또는 가공할 수 없습니다.

- 귀하는, 이 저작물의 재이용이나 배포의 경우, 이 저작물에 적용된 이용허락조건을 명확하게 나타내어야 합니다.
- 저작권자로부터 별도의 허가를 받으면 이러한 조건들은 적용되지 않습니다.

저작권법에 따른 이용자의 권리는 위의 내용에 의하여 영향을 받지 않습니다.

이것은 [이용허락규약\(Legal Code\)](#)을 이해하기 쉽게 요약한 것입니다.

[Disclaimer](#)

공학석사학위논문

# **Effects of unsteady flow on the tidal turbine farm layout optimization**

비정상유동이 조류발전단지 배치최적화에  
미치는 영향

2022 년 1 월

서울대학교 대학원

건설환경공학부

정원정

# Effects of unsteady flow on the tidal turbine farm layout optimization

비정상유동이 조류발전단지 배치최적화에 미치는 영향

지도 교수 황진환

이 논문을 공학석사 학위논문으로 제출함  
2022년 1월

서울대학교 대학원  
건설환경공학부  
정원정

정원정의 공학석사 학위논문을 인준함  
2022년 1월

위원장 \_\_\_\_\_ (인)

부위원장 \_\_\_\_\_ (인)

위원 \_\_\_\_\_ (인)

# ABSTRACT

Due to the global climate crisis and the air pollution, demand on the renewable energy is consequently increasing as one of the main efforts. Wind and solar energy are taking the lead on the renewable energy industry, and as of the next competitive resource, tidal power is estimated to have a huge potential, thanks to its high energy density and easily predictable characteristics.

Tidal power has not reached the practical level yet, due to financial challenges. In terms of reducing the cost and reach the competitive level of LCOE, the power extraction should be maximized within the constraints by conducting layout optimization of the turbines deployed, hence, understanding, and predicting the algorithm for layout optimization is necessary. The layout optimization for the tidal turbine is somewhat sophisticated, due to the unsteady tidal current condition in the nature, hence previous studies have found the problem under the steady condition. However, since the unsteadiness is a critical feature of the tidal current, there needs a study on the distinctive optimization characteristics under the unsteady condition.

This study aims to find the tidal turbine farm layout optimization problem under the simplified unsteady tidal current condition in the nature and identify if the tidal turbine farm layout optimization procedure under unsteady condition can converges to find the global optimum. A number of numerical experiments were handled during the study to find the general trend/pattern of convergence to the global optimum under the various unsteady condition, with variation in the amplitude and the direction.

The study first demonstrated the difference in the wake profile and the energy

production of a single turbine under steady & unsteady flow, to be used as the basic assumption when figuring out the characteristics of layout optimization procedure under unsteady condition. The study also demonstrated the insight of the optimized layout and the minimum velocity threshold that enables the optimization to converge to the globally optimized layout at a given tolerance under steady condition. Finally, generalization of the strategy for the tidal turbine farm layout optimization under the unsteady flow was presented by finding the difference in the optimization procedure between steady & unsteady flow. It has been discovered that optimal layout under unidirectional, unsteady flow condition is similar to the optimal layout under steady condition when it satisfies the minimum velocity threshold condition. However, optimal layout under bidirectional conditions was totally different to the optimal layout under unidirectional conditions, to consider the wake effect from both directions. Under the bidirectional flow condition, the turbines were found to be staggered with respect to each other in order to take advantage of local speedups between upwind turbines.

The numerical experiments were performed with OpenTidalFarm, an open-source solver for specific PDE-constrained, gradient-based optimization problems, especially those related to tidal farm design. The simulation domain was described as a rectangular farm, PDE is given as two-dimensional nonlinear shallow water equations, total power output is the target functional to be maximized, and turbine was parameterized as a bump function. Adjoint method was used as to compute the gradient for the optimization problem.

**Keywords:** Tidal turbine farm layout optimization, Unsteady tidal current, Gradient-based optimization, Shallow water equations, OpenTidalFarm

*Student Number:* 2019-21095

# TABLE OF CONTENTS

<b>ABSTRACT</b> .....	<b>i</b>
<b>TABLE OF CONTENTS</b> .....	<b>iv</b>
<b>List of Figures</b> .....	<b>vii</b>
<b>List of Symbol</b> .....	<b>xi</b>
<b>CHAPTER 1. INTRODUCTION</b> .....	<b>1</b>
<b>1.1 General introduction</b> .....	<b>1</b>
<b>1.2 Objective</b> .....	<b>2</b>
<b>CHAPTER 2. THEORETICAL BACKGROUDS</b> .....	<b>7</b>
<b>2.1 General evolution of the renewable energy</b> .....	<b>7</b>
<b>2.2 Tidal turbine farm</b> .....	<b>10</b>
<b>2.2.1 The physics of tide</b> .....	<b>10</b>
<b>2.2.2 The physics of tidal currents - unsteadiness</b> .....	<b>13</b>
<b>2.2.3 Tidal turbine</b> .....	<b>15</b>
<b>2.2.4 Tidal energy resources in Korea</b> .....	<b>17</b>
<b>2.3 Shallow water equation (SWE)</b> .....	<b>19</b>
<b>2.4 Gradient-based optimization using adjoint method</b> .....	<b>21</b>
<b>2.4.1 Problem formulation</b> .....	<b>22</b>
<b>2.4.2 The adjoint method</b> .....	<b>22</b>

<b>CHAPTER 3. METHODOLOGY .....</b>	<b>25</b>
<b>3.1 Numerical model description .....</b>	<b>25</b>
3.1.1 The design parameters.....	25
3.1.2 The PDE constraints .....	25
3.1.3 The turbine parameterization.....	26
3.1.4 The functional of interest .....	27
3.1.5 Box and inequality constraints.....	27
3.1.6 Optimization algorithm .....	28
<b>3.2 Experiment overview .....</b>	<b>29</b>
3.2.1 Experiment procedure.....	29
3.2.2 Experimental flow chart.....	31
<b>3.3 Simulation set-up .....</b>	<b>31</b>
3.3.1 Mesh domain .....	31
3.3.2 Boundary condition.....	33
3.3.3 Parameter settings.....	36
<b>CHAPTER 4. Test cases, Results and Discussions.....</b>	<b>39</b>
<b>4.1 Pilot Test 1: Steady &amp; Unsteady flow impact on a single turbine.....</b>	<b>39</b>
4.1.1 Wake behavior .....	39
4.1.2 comparison criterion between steady and unsteady flow based on the energy production .....	46
4.1.3 Conclusion of Pilot test 1 .....	48
<b>4.2 Pilot Test 2: Minimum velocity threshold (MVT) to converge to QGO and the concept of the optimized layout.....</b>	<b>49</b>
4.2.1 Test cases.....	49
4.2.2 Finding minimum threshold of velocity (MVT) .....	51
4.2.3 Insights on the optimized layout .....	55
4.2.4 Conclusion of Pilot test 2 .....	57
<b>4.3 Main test: Effect of unsteadiness in the optimization procedure compared to the steady condition .....</b>	<b>59</b>
4.3.1 Test cases.....	59

4.3.2 Optimal layout for each flow conditions .....	62
4.3.3 Strategy to obtain QGO for bidirectional flow condition.....	70
4.3.4 Conclusion of Main test .....	71
<b>CHAPTER 5. Conclusions .....</b>	<b>73</b>
<b>REFERENCES.....</b>	<b>76</b>
<b>국문초록 .....</b>	<b>80</b>

## List of Figures

<i>Figure 1.</i> Levelized cost of energy comparison between renewable energy source and the conventional energy source [11] .....	9
<i>Figure 2.</i> Tidal prediction curve for a semidiurnal tide over 24 h, with two high tides (HT) and two low tides (LT) with practically equal tidal ranges (Brest, France) [14] .....	11
<i>Figure 3.</i> Semidiurnal tide prediction curve over one lunation cycle (29 days) showing tidal range variations according to phases of the Moon (Brest, France) [14] .....	12
<i>Figure 4.</i> Concept figure of the axial-flow turbine [16] .....	16
<i>Figure 5.</i> The SeaGen-S 2MW turbine of Marine Current Turbines Ltd, raised above the surface of the water for inspection [17] .....	17
<i>Figure 6.</i> Spatial distribution of the 29-day tidal current observation-derived annual energy densities off the south and west coasts of Korea [18]. .....	18
<i>Figure 7.</i> $m$ containing design parameters in the turbine layout optimization problem .....	25
<i>Figure 8.</i> Flow chart of the optimization algorithm.....	28
<i>Figure 9.</i> Experimental flow chart.....	32
<i>Figure 10.</i> Simulation domain and the grid .....	33
<i>Figure 11.</i> Illustrations of boundary conditions for steady flow (left) and unsteady flow (right) at a given simulation domain.....	33
<i>Figure 12.</i> Turbine parameterized with bottom friction when the friction coefficient	

of 12 and the kinematic viscosity of  $3 \text{ m}^2/\text{s}$ . (A) A bottom friction plot across the channel domain; indicates the single turbine position; (B) 1D:  $\varphi(x|220 \leq x \leq 260, y = 160)$ ; (C) 2D:  $\varphi(x, y|220 \leq x \leq 260, 140 \leq y \leq 180)$ ..... 40

*Figure 13.* velocity magnitude field (A) and free surface elevation field (B) when a single turbine is deployed under a steady flow with  $u_0 = 0.95 \text{ m/s}$  from equation (25). Velocity magnitude field (C) and free surface elevation field (D) when a single turbine is deployed under a steady flow with  $u_0 = 1.56 \text{ m/s}$  from equation (29). ..... 41

*Figure 14.* velocity plot along the centerline of the channel when  $u_0 = 0.95 \text{ m/s}$  (red) and  $u_0 = 1.56 \text{ m/s}$  (green) from equation (29). Wake effect resulted in 15.8% reduction when  $u_0 = 0.95 \text{ m/s}$  and 19.2% reduction when  $u_0 = 1.56 \text{ m/s}$ . ..... 42

*Figure 15.* wake effect for 5 different inlet velocities; wake effect tends to get higher when the inlet velocity increases. .... 42

*Figure 16.* average velocity and average free surface elevation plot over time domain under an unsteady flow with  $\eta_0 = 1.8 \text{ m}$  from equation (36). ..... 43

*Figure 17.* velocity magnitude field when a single turbine is deployed under an unsteady flow with  $\eta_0 = 1.8 \text{ m}$  from equation (36); each figure captured after (A)  $T/8$ , (B)  $T/4$ , (C)  $T/2$ , (D)  $3T/4$ , and (E)  $7T/8$  since the flow has started. .... 44

*Figure 18.* velocity plot along the centerline of the channel after (A)  $T/8$ , (B)  $T/4$ , (C)  $3T/4$ , and (D)  $7T/8$  since the flow has started. .... 45

*Figure 19.* wake effect with regards to the inlet velocities, which differ by each time step when a single turbine is deployed under an unsteady flow with  $\eta_0 = 1.8 \text{ m}$

from equation (36). .....	45
<i>Figure 20.</i> difference in the energy production between the unsteady sinusoidal flow with maximum velocity of 1.3 m/s and the steady flow with 0.95 m/s velocity. A cyclic-averaged single turbine production was equal in both condition with 0.18 MW (left); Difference in the energy production between the unsteady sinusoidal flow with maximum velocity of 2.1 m/s and the steady flow with 1.56 m/s velocity. A cyclic-averaged single turbine production was equal in both condition with 0.67 MW (right). .....	46
<i>Figure 21.</i> relationship between steady velocity and unsteady maximum velocity when the energy production is the same over a tidal period. ....	47
<i>Figure 22.</i> optimized layout under the steady flow condition with different $u_0$ from equation (29) for different number of turbines .....	52
<i>Figure 23.</i> production plot along the optimization procedure, for different flow speeds, for each different number of turbines.....	53
<i>Figure 24.</i> power production increase, compared to the production under initial layout; production increase for MVT is indicated in yellow and the corresponding velocities are on the top of the bar .....	54
<i>Figure 25.</i> Optimal layout (QGO) and the velocity contour for each number of turbines.....	56
<i>Figure 26.</i> Free surface elevation contour for the optimal layout of $N = 7$ case ..	57
<i>Figure 27.</i> layout optimization for different flow conditions when $N = 6$ and $N = 7$ .....	63
<i>Figure 28.</i> layout optimization for different flow conditions when $N = 8$ and $N =$	

9 .....	64
<i>Figure 29.</i> tidal farm production under the bidirectional flow condition for layouts optimized under different flow conditions when $\eta_0 = 4$ m and $N = 7$ .....	67
<i>Figure 30.</i> velocity magnitude contour for each layout optimized under three different flow conditions when $\eta_0 = 4$ m and $N = 7$ ; (A) steady flow, (B) unsteady, unidirectional flow, (C) unsteady, bidirectional flow at the highest velocity peak in positive direction and (D) at the highest velocity peak in negative direction .....	68
<i>Figure 31.</i> Difference in the first step of optimization for each flow conditions when $\eta_0 = 4$ m; it is clearly very much different under the bidirectional flow .....	68
<i>Figure 32.</i> tidal farm production under the bidirectional flow condition for layouts optimized under different flow conditions when $\eta_0 = 4$ m and (A) $N = 6$ and (B) $N = 8$ .....	69
<i>Figure 33.</i> reoptimized layout under bidirectional flow conditions when (A) $\eta_0 = 4$ m and $N = 6$ , (B) $\eta_0 = 4$ m and $N = 7$ , (C) $\eta_0 = 6$ m and $N = 8$ , velocity magnitude contour for $N = 7$ when (D) positive direction (E) negative direction	71

# List of Symbol

## Background theory

$c$	Velocity of progress of the wave
$g$	Gravitational acceleration
$\eta$	Free surface elevation
$\eta_0$	Mean sea level
$f_j$	Node factor of the j-th constituent of each tide
$H_j$	Amplitude of the j-th constituent of each tide
$\omega_j$	Frequency of the j-th constituent of each tide
$\theta_j$	Nodal phase of the j-th constituent of each tide
$\delta_j$	Phase of the j-th constituent of each tide
$H$	Mean water depth
$u$	Horizontal velocity in x direction
$v$	Horizontal velocity in y direction
$\nu$	Kinematic viscosity coefficient
$k$	Wave number
$\rho$	Fluid density
$A_d$	Total device area
$C_p$	Turbine power coefficient
$u_\infty$	Free-stream flow speed

$P$	Power extraction from a turbine
$P_d$	Power density from a turbine
$E_d$	Energy density from a turbine
$E_{Md}$	Monthly energy density
$E_{Ad}$	Annual energy density
$f$	Coriolis coefficient
$b$	Viscous drag coefficient
$J$	Functional of interest
$m$	Design parameters
$F$	PDE operator
$z$	Solution of the PDE operator
$b_l$	Lower bound constraint
$b_u$	Upper bound constraint
$g(m)$	Additional restrictions of the optimization
$p$	Perturbation in the flow field
$\lambda$	Adjoint solution

## **Methodology**

$c_b$	Quadratic bottom friction of the simulation
$c_t$	Turbine parameterization
$\psi_{p,r}$	Bump function of the turbine
$r$	Support radius of the bump function
$p$	Center of the bump function
$K$	Friction coefficient of the turbine parameterization
$N$	Number of turbines
$C_i$	Fiction function of a single turbine
$T$	Final time of the simulation time domain
$d_{\min}$	Minimum distance between the turbines
$Fr$	Froude number
$D$	Hydraulic depth
$P$	Tidal period
$A$	Amplitude
$\phi$	Phase leg

# CHAPTER 1. INTRODUCTION

## 1.1 General introduction

Due to the global climate crisis and the air pollution, efforts to protect the environment and prevent the global warming are increasing. Demand on the renewable energy is consequently increasing as one of the main efforts, hence renewable energy is expected to take a significant role as an alternative electricity generation source in the near future.

Wind and solar energy are taking the lead on the renewable energy industry with their cost-competitive feature, owing to the large-scale development and the highly developed technology. As of the next competitive resource, one of the ocean-related renewable energy sources, tidal power, generated from the tide, has a potential of highly reliable renewable energy source with several reasons:

- Easily predictable, since the tidal flows are generated by astronomical forces
- Less dependent on the weather condition
- Inexpensive maintain cost
- High energy density compared to the other renewable energy forms

Tidal power has not reached the practical level yet, due to financial challenges, but recent developments in energy converter technology are reducing the cost of tidal power, bringing it closer to becoming a competitive industry. The global tidal resource which could be exploited and converted to electrical power has been

estimated at several hundred gigawatts.

Furthermore, within the past few years, new technology to extract kinetic power from tidal streams has reached an advanced demonstration phase. This approach uses free stream turbines to extract kinetic power from moving water and, unlike a barrage, does not require environmentally damaging impoundment behind a dam [1], thus has made the tidal energy more beneficial both environmentally and industrialization wise.

To reduce the cost and reach the competitive level of LCOE, first, the turbines will need to be operated in large arrays and second, the power extraction should be maximized within the constraints by conducting layout optimization of the turbines deployed, hence, understanding, and predicting the algorithm for tidal turbine farm layout optimization is necessary.

## **1.2 Objective**

The concept of turbine layout optimization was first introduced for wind turbines. When a turbine extracts power from the wind, it generates a “wake” of turbulence that propagates downwind, so that the wind speed and therefore the power extraction from the turbines affected are reduced. In large wind farms wake effects lead to considerable power loss, and thus it is desirable to minimize them in order to maximize the expected power output. Wind turbine layout optimization problem consists of finding the turbine positioning that maximizes the expected power production.

The systematic approaches to wind turbine placement were first proposed by Mosetti et al. [2]. The optimization was made by associating a windfarm simulation model based on wake superposition with a genetic algorithm. Starting from genetic algorithm in mid-1990, various studies on the wind farm layout optimization problem has emerged. Wan et al. [3], solved the optimization problem with a particle swarm optimization algorithm based on penalty functions, and Bilbao & Alba [4] used Simulated annealing algorithm to search the optimal positions in the large landscape of possible positions. Recently, higher-fidelity CFD flow models have been used in a limited range of wind plant optimization applications. The Technical University of Denmark has developed TOPFARM [5], which employs an improved wake model 30 (the dynamic wake meandering model) as well as a parabolic Navier-Stokes solver. TOPFARM uses a hybrid optimization approach that combines sequential linear programming (SLP) with gradient-free genetic algorithms. The genetic algorithm is used to find the neighborhood of the global optimum, and then the gradient-based SLP algorithm completes the optimization. However, the genetic algorithm step penalizes large design spaces, limiting TOPFARM to relatively small wind plants.

These gradient-free approaches, however, yields a number of model evaluations which would be infeasible for a more complex PDE-based model such as the optimization problem in the tidal farm. Therefore, gradient-based optimization should be introduced in the tidal turbine layout optimization problem. This gradient-based approach also permits the use of high-dimensional control spaces, thereby providing optimized layouts of arbitrary complexity (i.e., optimized layouts are not restricted to grids or any other regular arrangement).

Funke et al. [6] proposed a novel technique to formulate the PDE-constrained gradient-based optimization problem automatically for a tidal farm using the adjoint method for the fast and scale-independent evaluation of a functional derivative. However, the gradient-based optimization has an inherent drawback in that its solution is highly sensitive to the initial solution and additionally, solutions are likely to be stuck in the local minima, hence the convergence of solutions to the global optima cannot be guaranteed, [7]. Han et al. [8] have conducted various numerical experiments by varying number of turbines and optimization constraints and explained some of the underlying general trend of the optimal array layout. The study also demonstrates that the initial layout is critical for the gradient-based algorithm to overcome its inherent limitation of convergence to local optima and to ensure the convergence to quasi-global optimum (QGO)<sup>1</sup> at a low computational cost. The limitation of the study, however, is that it has found a trend only in the ideal condition with steady unidirectional flow.

In the present study, we use adjoint techniques to enable gradient-based optimization of tidal turbine locations within a farm, subject to realistic unsteady flow field. A sinusoidal Flather boundary condition was introduced at the channel inlet and outlet, rather than prescribing fixed wake behaviors as in steady flow conditions. We

---

<sup>1</sup> As the complexity of a problem increases, it becomes difficult to prove that the obtained solution is a global optimum. As an alternative, a concept of quasi-global optimum (QGO) was introduced, as an attempt to reconcile the cost and accuracy by using a sub-optimal solution that can be regarded as a surrogate of the true global optimum [8].

further demonstrate layout optimization for the different flow speed conditions based on the realistic velocities, going beyond the uniform speed optimization considered previously [8]. The resulting optimization framework thus represents a novel application of adjoint techniques to the optimization of utility-scale tidal stream turbine farms under the simplified unsteady condition in the nature, and identify if the tidal turbine farm layout optimization procedure under unsteady condition finally converges to find the QGO. The present study aims to unveil the problem mainly by answering the following questions:

- (i) Demonstrate the difference in the wake profile and the energy production of a single turbine under steady & unsteady flow
- (ii) Demonstrate the insight of the optimized layout (QGO) and the minimum velocity threshold that enables the optimization to converge to the globally optimized layout at a given tolerance
- (iii) Generalize the strategy for the tidal turbine farm layout optimization under the flow with unsteadiness by finding the difference in the optimization procedure between steady & unsteady flow

	<b>Reference</b>	<b>Topic</b>	<b>Optimization method</b>	<b>Flow condition</b>
Wind farm	Mosetti et al. (1994)	Optimization of wind turbine positioning in large windfarms by means of a genetic algorithm	Gradient-free	Steady flow
	Wan et al. (2010)	Optimal micro-siting of wind farms by particle swarm optimization	Gradient-free	Steady flow
	Bilbao & Alba (2009)	Simulated annealing for optimization of wind farm annual profit	Gradient-free	Steady flow
	Larsen et al. (2011)	TOPFARM - next generation design tool for optimisation of wind farm topology and operation	Hybrid optimization approach	Steady flow
Tidal farm	Funke et al. (2014)	Tidal turbine array optimisation using the adjoint approach	Gradient-based, adjoint method	Steady flow
	Noel (2012)	A new gradient based particle swarm optimization algorithm for accurate computation of global minimum	Gradient-based, particle swarm algorithm	-
	Han et al. (2021)	Optimal configuration of a tidal current turbine farm in a shallow channel	Gradient-based, adjoint method	Steady flow
	Polagye et al. (2008)	Effect of large-scale kinetic power extraction on time-dependent estuaries	Two-way effect	Unsteady flow
	<b>Present study (2021)</b>	Effects of unsteady flow on the tidal turbine farm layout optimization	Gradient-based, adjoint method	Unsteady flow

## **CHAPTER 2. THEORETICAL BACKGROUDS**

### **2.1 General evolution of the renewable energy**

Evidence shows that our planet has been getting hotter. The warmest 20 years on record have been in the last 22 years according to the World Meteorological Organization and the warmest four were all very recent: 2015 to 2018. Global average temperatures are now 1 °C higher than in the pre-industrial era. A degree doesn't sound like a lot, but the reality is that this incremental warming already appears to be having a negative impact. There has been a prediction that if recent trends continue, global temperatures will increase by as much as 3-5 °C by 2100. Even with this tiny rise in global temperatures we are feeling the effects of climate change, with erratic weather patterns, including: heatwaves; floods and severe storms; loss of polar ice; and, rising sea levels. This will only get worse if global warming intensifies [9].

In accordance with this urgent global issue, several countries including South Korea have introduced targets to achieve net-zero emissions by 2050. Net-zero means achieving a balance between the greenhouse gases put into the atmosphere and those taken out, which is important as it is the best way to tackle climate emergency by reducing global warming [10].

Electrical generation is the leading cause of industrial air pollution since most of the electricity comes from coal, nuclear, and the other non-renewable power plants.

Producing energy from these resources takes a severe toll on our environment, polluting our air, land, and water. Meanwhile, renewable energy sources can be used to produce electricity with fewer environmental impacts. To be more specific, it is possible to produce electricity from renewable energy sources without producing CO<sub>2</sub>, which is the main reason for global climate change.

Therefore, to target net-zero emissions, to limit the emissions of carbon we produce, the demand of renewable energy sources as the alternative of existing conventional energy sources are rapidly increasing hence the study on the renewable energy source itself and the corresponding technology is highly important.

The main challenge for renewable industry is the cost of energy, however, Lazard's latest annual Levelized Cost of Energy Analysis (LCOE), *Figure 1*, shows that as the cost of renewable energy continues to decline, certain technologies (e.g., onshore wind and utility-scale solar), which became cost-competitive with conventional generation several years ago on a new-build basis, continue to maintain competitiveness with the marginal cost of selected existing conventional generation technologies. The cost reduction could happen thanks to the technology development in energy extraction and the industrialization due to the bigger scale it reaches [11].

There still remains the financial challenges for many other renewable energy sources, however, if they have the capability of the cost reduction that wind and solar energy has gone through, they can also be used as the key energy source to reach net-zero at the designated year.

## Levelized Cost of Energy Comparison—Unsubsidized Analysis

Selected renewable energy generation technologies are cost-competitive with conventional generation technologies under certain circumstances



Source: Lazard estimates.

Note: Here and throughout this presentation, unless otherwise indicated, the analysis assumes 60% debt at 8% interest rate and 40% equity at 12% cost. Please see page titled "Levelized Cost of Energy Comparison—Sensitivity to Cost of Capital" for cost of capital sensitivities. These results are not intended to represent any particular geography. Please see page titled "Solar PV versus Gas Peaking and Wind versus CCGT—Global Markets" for regional sensitivities to selected technologies.

- (1) Unless otherwise indicated herein, the low case represents a single-axis tracking system and the high case represents a fixed-tilt system.
- (2) Represents the estimated implied midpoint of the LCOE of offshore wind, assuming a capital cost range of approximately \$2,600 – \$3,675/kW.
- (3) The fuel cost assumption for Lazard's global, unsubsidized analysis for gas-fired generation resources is \$3.45/MMBTU.
- (4) Unless otherwise indicated, the analysis herein does not reflect decommissioning costs, ongoing maintenance-related capital expenditures or the potential economic impacts of federal loan guarantees or other subsidies.
- (5) Represents the midpoint of the marginal cost of operating fully depreciated gas combined cycle, coal and nuclear facilities, inclusive of decommissioning costs for nuclear facilities. Analysis assumes that the salvage value for a decommissioned gas combined cycle or coal asset is equivalent to its decommissioning and site restoration costs. Inputs are derived from a benchmark of operating gas combined cycle, coal and nuclear assets across the U.S. Capacity factors, fuel, variable and fixed operating expenses are based on upper- and lower-quartile estimates derived from Lazard's research. Please see page titled "Levelized Cost of Energy Comparison—Renewable Energy versus Marginal Cost of Selected Existing Conventional Generation" for additional details.
- (6) High end incorporates 90% carbon capture and storage. Does not include cost of transportation and storage.
- (7) Represents the LCOE of the observed high case gas combined cycle inputs using a 20% blend of "Blue" hydrogen, (i.e., hydrogen produced from a steam-methane reformer, using natural gas as a feedstock, and sequestering the resulting CO<sub>2</sub> in a nearby saline aquifer). No plant modifications are assumed beyond a 2% adjustment to the plant's heat rate. The corresponding fuel cost is \$5.20/MMBTU.
- (8) Represents the LCOE of the observed high case gas combined cycle inputs using a 20% blend of "Green" hydrogen, (i.e., hydrogen produced from an electrolyzer powered by a mix of wind and solar generation and stored in a nearby salt cavern). No plant modifications are assumed beyond a 2% adjustment to the plant's heat rate. The corresponding fuel cost is \$10.05/MMBTU.

Figure 1. Levelized cost of energy comparison between renewable energy source and the conventional energy source [11]

## 2.2 Tidal turbine farm

### 2.2.1 The physics of tide

Tides are the rise and fall of sea levels caused by the combined effects of the gravitational forces exerted by the Moon and the Sun, and the rotation of the Earth. The motion of the sun and the moon relative to the earth is so complicated that the system of gravitational tidal forces changes greatly in the course of time, which leads to the complicated yet repeating variation in tide. Experience has shown, however, that the tides can be considered as composed mainly of a series of harmonic oscillations, or *partial tides*, having the periods of the tide-producing forces [12].

Among many decompositions, there exist 4 main constituents that are actually important:  $M_2$ ,  $S_2$ ,  $K_1$ , and  $O_1$ . The moon, which has the greatest influence on the tidal force, orbits around the Earth every 24 hours and 50 minutes, causing two flood tides and two ebb tides, resulting 12 hours and 25 minutes periods for each. This is known as Principal lunar semidiurnal,  $M_2$  and is the most important period when understanding the tidal mechanism. Lunar diurnal,  $O_1$ , also created by the Moon's orbital cycle, has a period of 25.82 hours, with an effect of 0.415 compared to the  $M_2$  constituent. Principal solar semidiurnal,  $S_2$ , which is driven by the relative motion of the Sun due to the orbital movement of the Earth, has a 12-hour period with an effect of 0.466 compared to the  $M_2$  constituent. Finally, another kind of Lunar diurnal,  $K_1$ , driven by the difference in the relative positioning of the Sun and the Moon, has 23.93 hours of period, and the effect is 0.548 compared to  $M_2$  [13].

This can be easily observed from the measurement of sea level variation, which

consist of a number of sinusoidal waves with different periods and amplitudes.

Figure 2 shows four extremes, with each minimum representing low water (LW) and each maximum being high water (HW). The short period at high or low water during which there are no appreciable height variations is called stand. From low to high water, the height rises during the flood or rise phase, and it declines from high to low water during the ebb or fall phase [14].

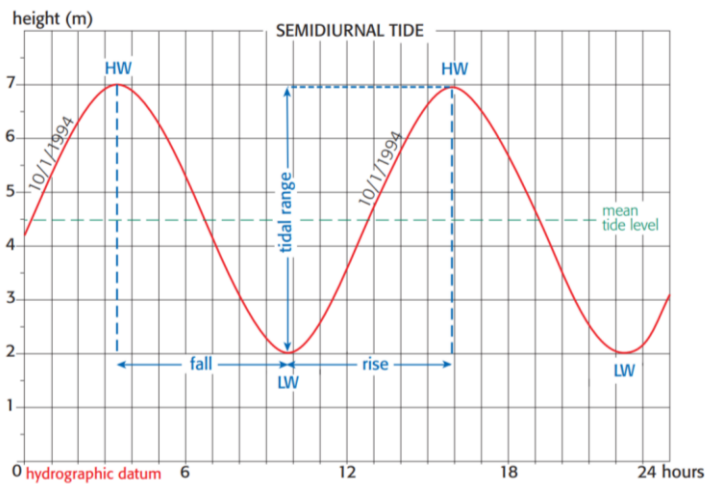


Figure 2. Tidal prediction curve for a semidiurnal tide over 24 h, with two high tides (HT) and two low tides (LT) with practically equal tidal ranges (Brest, France) [14]

Figure 3 presents a general example of a semidiurnal tide curve over a lunation cycle of around 30 days. The tidal range variations are very typical, going from a minimum during the neap tide (NT) to a maximum during the spring tide (ST). The tidal range increases during the priming phase and declines during the lagging phase. The age of tide is the time interval between phases of the moon and the tidal minima or maxima that immediately follows. The full and new moons (FM and NM) are

followed by spring tides, while the first and last quarter moons (FQ and LQ) are followed by neap tides [14].

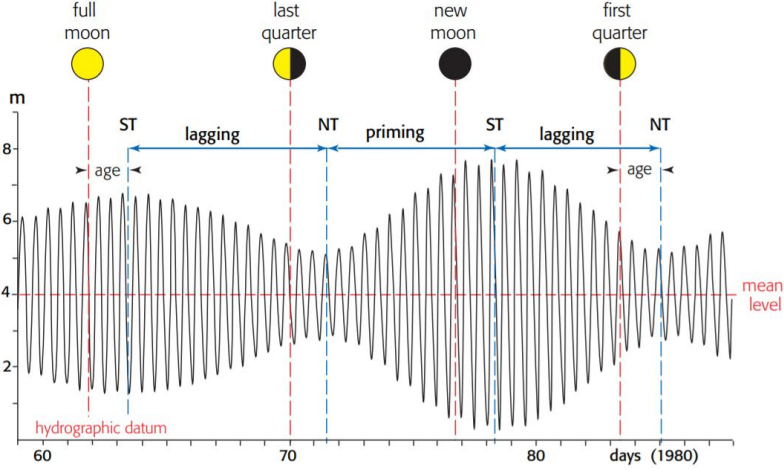


Figure 3. Semidiurnal tide prediction curve over one lunation cycle (29 days) showing tidal range variations according to phases of the Moon (Brest, France) [14]

Decomposition of regular partial sinusoidal waves from observed tide is called tidal harmonic analysis. Harmonic analysis was initiated by Laplace, William Thomson, and George Darwin, and the presented formula was developed by A.T. Doodson. The harmonic analysis can be expressed as

$$\eta(t) = \eta_0 + \sum_{j=1}^m f_j H_j \cos(\omega_j t + \theta_j - \delta_j) = \eta_0 + \sum_{j=1}^m R_j \cos(\omega_j - \phi_j), \quad (1)$$

where  $\eta(t)$  is the estimated tidal height at time  $t$ ,  $\eta_0$  is the mean sea level,  $f_j$ ,  $H_j$ ,  $\omega_j$ ,  $\theta_j$ ,  $\delta_j$  are the node factor, amplitude, frequency, nodal phase and the phase of the  $j$ -th constituent of each tide.  $m$  is the number of the tidal constituents that were used [13].

### 2.2.2 The physics of tidal currents - unsteadiness

Tidal currents, or tidal flows occur in conjunction with the rise and fall of the tide. The vertical motion of the tides near the shore causes the water to move horizontally, creating currents. The tidal currents will therefore exhibit different character in different areas, depending upon the character of the tides, and will, in a given locality, pass through cyclic changes corresponding to those of the tide [12].

In order to find simple equations that describe the tidal currents, it is necessary to start with continuity equation and momentum equations. Disregarding friction and the rotation of the earth, placing the  $x$ -axis in the direction of progress of the tide wave, and assuming constant depth, continuity equation can be rewritten in 2-D form as

$$\frac{\partial \eta}{\partial t} + (H + \eta) \frac{\partial u}{\partial x} + (H + \eta) \frac{\partial v}{\partial y} = 0, \quad (2)$$

and the momentum equations can be written as

$$\begin{aligned} \frac{\partial u}{\partial t} + u \frac{\partial u}{\partial x} + v \frac{\partial u}{\partial y} + g \frac{\partial \eta}{\partial x} &= \nu \left( \frac{\partial^2 u}{\partial x^2} + \frac{\partial^2 u}{\partial y^2} \right), \\ \frac{\partial v}{\partial t} + u \frac{\partial v}{\partial x} + v \frac{\partial v}{\partial y} + g \frac{\partial \eta}{\partial y} &= \nu \left( \frac{\partial^2 v}{\partial x^2} + \frac{\partial^2 v}{\partial y^2} \right), \end{aligned} \quad (3)$$

where  $\eta$  is the free-surface elevation, which is the tidal wave height in this study,  $H$  is the mean water depth,  $u$  and  $v$  are the horizontal velocity in the  $x$  and  $y$  direction respectively,  $g$  is the gravitational acceleration, and  $\nu$  is the kinematic viscosity.

The momentum equations describing progressive sinuous long wave can be written in the simpler form if neglecting the terms quadratic in  $u$  and  $v$ , which represent the effect of bulk advection, and are small compared to the other terms. Assuming also

that the tidal wave height is very small compared to the mean water depth ( $\eta \ll H$ ), we can derive equation (4):

$$\begin{aligned}\frac{\partial \eta}{\partial t} + H \left( \frac{\partial u}{\partial x} + \frac{\partial v}{\partial y} \right) &= 0, \\ \frac{\partial u}{\partial t} + g \frac{\partial \eta}{\partial x} &= 0, \\ \frac{\partial v}{\partial t} + g \frac{\partial \eta}{\partial y} &= 0.\end{aligned}\tag{4}$$

Since  $y$ -component has a very small variability across the channel in our case of rectangular channel with one directional flow in the inlet boundary, above three equations can be reduced to two as in equation (5):

$$\begin{aligned}\frac{\partial \eta}{\partial t} + H \frac{\partial u}{\partial x} &= 0, \\ \frac{\partial u}{\partial t} + g \frac{\partial \eta}{\partial x} &= 0.\end{aligned}\tag{5}$$

For a progressive wave, equation (5) have solutions of tidal currents in the small amplitude assumptions as

$$\begin{aligned}\eta &= \eta_0 \cos(kx - \omega t), \\ u &= g \frac{k}{\omega} \eta_0 \cos(kx - \omega t) = c \frac{\eta_0}{H} \cos(kx - \omega t) = \eta_0 \sqrt{\frac{g}{H}} \cos(kx - \omega t).\end{aligned}\tag{6}$$

where  $\eta_0$  is the amplitude of a tidal constituent,  $\omega (= \frac{2\pi}{T})$  is the tidal frequency, and  $k (= \frac{1}{\lambda})$  is the wave number, and  $c (= \sqrt{gH})$  is the velocity of progress of the wave. These  $u$  and  $\eta$  are used for the boundary inputs in this study and will also be presented as the external values of the solution.

Therefore, the velocity reaches its maximum in the direction of progress at high

tide ( $\eta = \eta_0$ ) and its maximum in the opposite direction at low tide ( $\eta = -\eta_0$ ). The tidal current is alternating, changing its direction every half period.

When a tidal current move toward the land and away from the sea, it “floods.” When it moves toward the sea away from the land, it “ebbs.” These tidal currents that ebb and flood in opposite directions are called “rectilinear” or “reversing” currents [15].

Rectilinear tidal currents, which typically are found in coastal rivers and estuaries, experience a “slack water” period of no velocity as they move from the ebbing to flooding stage, and vice versa. After a brief slack period, which can range from seconds to several minutes and generally coincides with high or low tide, the current switches direction and increases in velocity.

### 2.2.3 Tidal turbine

Tidal axial turbines extract energy from a moving fluid; consequently, they are somewhat analogous to wind turbines. The amount of power a turbine can extract from an unbounded fluid flow can be described mathematically using momentum theory (also known as actuator disc theory) [16]:

$$P = \frac{1}{2} \rho A C_p u_\infty^3. \quad (7)$$

where  $\rho$  is the fluid density,  $A$  is the total device area,  $C_p$  is the turbine power coefficient, and  $u_\infty$  is the free-stream flow speed. This leads to a simple calculation of turbine power density (the power produced per  $\text{m}^2$  of total device area):

$$P_d = \frac{P}{A} = \frac{1}{2} \rho C_p u_\infty^3. \quad (8)$$

Using equation (8), the energy density over a certain period of time  $T$  is given by:

$$E_d = \int_0^T P_d dt. \quad (9)$$

We can easily find from the equation (8) that the power production is very much dependent on the flow speed and thus deploying turbines in a high velocity region is highly important.

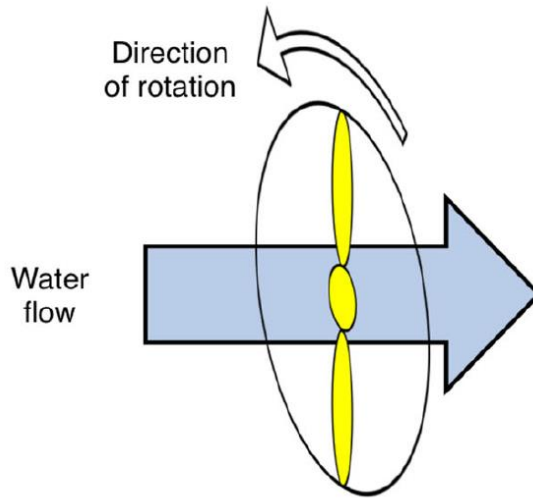


Figure 4. Concept figure of the axial-flow turbine [16]

Table 1 is summarizing the performance characteristics of several commercial axial-flow turbines, which was used as the reference when modelling turbines within the simulation for the study and Figure 5 is showing one of the tidal turbines by Marine Current Turbines Ltd., extracting the power following the actuator disk theory briefly introduced in equation (7) - (9).

Table 1. Performance characteristics of selected commercial axial-flow turbines [16]

Developer Device	Atlantis AR1000	Bourne RiverStar	MCT SeaGen S	Verdant Gen5	Voith 1 MW test
Rated power (W)	$1.00 \times 10^6$	$5.00 \times 10^4$	$2.00 \times 10^6$	$1.68 \times 10^3$	$1 \times 10^6$
Rated flow speed (m/s)	2.65	2.05	2.40	2.59	2.90
No. of rotors (-)	1	1	2	3	1
Rotor diameter (m)	18.0	6.09	20.0	5.00	16.0
Rotor swept area (m <sup>2</sup> )	254	29	314	20	201
Rated $C_p$	0.41	0.39	0.45	0.35	0.40



Figure 5. The SeaGen-S 2MW turbine of Marine Current Turbines Ltd, raised above the surface of the water for inspection [17]

#### 2.2.4 Tidal energy resources in Korea

There are several demonstration tidal energy projects in various stages of development around the world and Korea is one of the countries investigating into it. Byun et al. [18] comprises a preliminary assessment of the tidal current energy resources of southern and western Korea, and found a spatial energy density

distribution based on the current velocity observation at 264 stations around the coast.

In the study, monthly energy densities ( $E_{Md}$ ) from the  $k$ -day observation data sets were calculate as:

$$E_{Md} = \frac{1}{n} \sum_{D=1}^k \sum_{h=1}^{24} \sum_{m=1}^n [P_d]_{m,h,D}, \quad (10)$$

where  $m$ ,  $h$ , and  $D$  indicate minutes, hours, and days, respectively.  $k$  used was 29 and

$n = \frac{60 \text{ min}}{\Delta t \text{ min}}$  with  $\Delta t$  stands for observation interval within the study. Subsequently,

annual energy densities ( $E_{Ad}$ ) were estimated by:

$$E_{Ad} = 365 \left( \frac{E_{Md}}{k} \right). \quad (11)$$

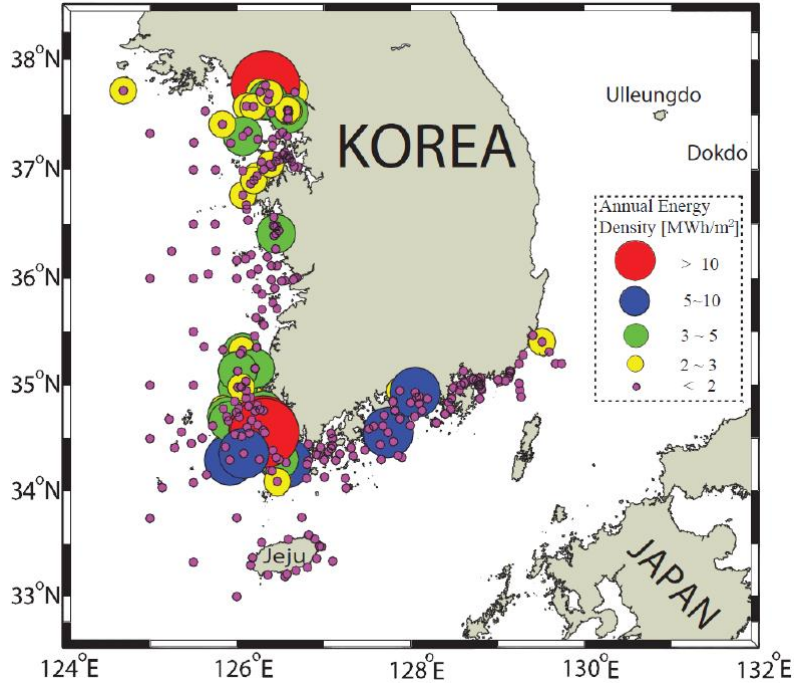


Figure 6. Spatial distribution of the 29-day tidal current observation-derived annual energy densities off the south and west coasts of Korea [18].

The results by Byun et al. reveal that environments exhibiting very high annual tidal current energy densities are likely to be relatively rare around Korea. *Figure 6* show the greatest concentration of high-energy density sites was found off the coast of Jeonnam Province: including the highest energy density of  $53 \text{ MWh} \cdot \text{m}^{-2}$  in Uldolmok;  $9 \text{ MWh} \cdot \text{m}^{-2}$  in the Geocha Waterway; and  $6.9 \text{ MWh} \cdot \text{m}^{-2}$  in the Jangjuk Waterway. In line with the attractive condition, Uldolmok Tidal Current Power Pilot Plant is currently operating as the first tidal turbine project in Korea.

### **2.3 Shallow water equation (SWE)**

The Shallow water equations (SWE) are derived from depth-integrating the Navier–Stokes equations, where the horizontal length scale is much greater than the vertical length scale. Under this condition, conservation of mass implies that the vertical velocity scale of the fluid is too small to be compared with the horizontal velocity scale. It can be shown from the momentum equation that vertical pressure gradient is nearly hydrostatic, and that horizontal pressure gradient occurs only due to the displacement of the pressure surface which implies that the horizontal velocity field is constant throughout the depth of the fluid. Vertical integration allows the vertical velocity terms to be neglected from the Navier-Stokes equations.

Several situations in fluid dynamics, especially in the region where tidal farms are implemented, the horizontal length scale is much greater than the vertical length scale in general, hence shallow water equations are widely applicable for the study.

In the case of a horizontal bed, with negligible Coriolis forces, frictional and

viscous forces, the shallow water equation can be derived from the mass conservation equation and momentum conservation equations and presented in the conservative form as [19]:

$$\begin{aligned}\frac{\partial(\rho h)}{\partial t} + \frac{\partial(\rho h u)}{\partial x} + \frac{\partial(\rho h v)}{\partial y} &= 0, \\ \frac{\partial(\rho h u)}{\partial t} + \frac{\partial}{\partial x} \left( \rho h u^2 + \frac{1}{2} \rho g h^2 \right) + \frac{\partial(\rho h u v)}{\partial y} &= 0, \\ \frac{\partial(\rho h v)}{\partial t} + \frac{\partial(\rho h u v)}{\partial x} + \frac{\partial}{\partial y} \left( \rho h v^2 + \frac{1}{2} \rho g h^2 \right) &= 0.\end{aligned}\tag{12}$$

where  $h$  is the total fluid column height,  $u$  and  $v$  are fluid's horizontal flow velocity for  $x$  and  $y$  direction, respectively,  $g$  is the gravitational acceleration and  $\rho$  is the fluid density.

Expanding the derivatives in the above using the product rule, the non-conservative form of the shallow-water equations is obtained [19]. The appropriate terms for Coriolis, frictional and viscous forces are included this time.

$$\begin{aligned}\frac{\partial \eta}{\partial t} + \frac{\partial}{\partial x} ((H + \eta)u) + \frac{\partial}{\partial y} ((H + \eta)v) &= 0, \\ \frac{\partial u}{\partial t} + u \frac{\partial u}{\partial x} + v \frac{\partial u}{\partial y} - f v &= -g \frac{\partial \eta}{\partial x} - b u + \nu \left( \frac{\partial^2 u}{\partial x^2} + \frac{\partial^2 u}{\partial y^2} \right), \\ \frac{\partial v}{\partial t} + u \frac{\partial v}{\partial x} + v \frac{\partial v}{\partial y} + f u &= -g \frac{\partial \eta}{\partial y} - b v + \nu \left( \frac{\partial^2 v}{\partial x^2} + \frac{\partial^2 v}{\partial y^2} \right).\end{aligned}\tag{13}$$

where  $\eta$  is the free surface elevation,  $H$  is the mean water depth,  $f$  is the Coriolis coefficient associated with the Coriolis force,  $b$  is the viscous drag coefficient and  $\nu$  is the kinematic viscosity.

## 2.4 Gradient-based optimization using adjoint method

Optimization algorithms can be divided into two categories: gradient-free and gradient-based algorithms.

Gradient-free optimization algorithms use the functional of interest as a black box. They proceed by evaluating the functional at many points in parameter space and use the values to decide which areas merit further exploration. By contrast, gradient-based optimization algorithms use the derivatives of the functional of interest with respect to the parameters to update the position in parameter space at each iteration. By adding this additional derivative information, gradient-based optimization can lead to a significant reduction in the number of iterations required compared to the gradient-free optimization. Therefore, gradient-based optimization is much more attractive in the optimization problem in a large scale, such as this study when optimizing layout for number of turbines to be deployed [6].

The main difficulty of applying gradient-based methods is that the implementation of the gradient computation can be difficult for complex models, as it involves differentiating through the solution of a partial differential equation – non-linear shallow water equation for the case in this study. In the 1970s, a method based on the adjoint state has been introduced in the theory of inverse problems by Chavent (1974) to efficiently compute the gradient of a functional. This approach originated from control theory by Lions (1972). Several authors in geophysics have applied this method, for instance, Lailly (1983), B´ecache (1992), Chavent & Jacewitz (1995), Plessix et al. (1999) and Shen et al. (2003) [20].

### 2.4.1 Problem formulation

PDE-constrained optimization problem in general follows the abstract form:

$$\begin{aligned} \max_{z,m} J(z, m) \\ \text{subject to } F(z, m) = 0, \\ b_l \leq m \leq b_u, \\ g(m) \leq 0, \end{aligned} \tag{14}$$

where  $J(z, m) \in \mathbb{R}$  is the functional of interest,  $m$  are the design parameters,  $F(z, m)$  is a PDE operator parameterized by  $m$  with solution  $z$ ,  $b_l$  and  $b_u$  are the lower and upper bound constraints for the design parameters, and  $g(m)$  enforces additional restrictions on the design parameters [6].

In this study, shallow water equations were expressed in the form of  $F(z, m)$ .  $z = (u, \eta)$  is the solution of the shallow water equations where  $u$  represents horizontal velocity and  $\eta$  represents free-surface elevation.  $m$  contains the position of the turbines, and the bounds  $b_l$  and  $b_u$  are used to enforce that the turbines remain in a prescribed area. Finally,  $g(m)$  is used to enforce a minimum distance between any two turbines, hence is able to prevent any overlapping between the turbines during the optimization process and leads to higher practicality.

### 2.4.2 The adjoint method

The adjoint method is a numerical method for efficiently computing the gradient of a function or an operator in a numerical optimization problem. While the other optimization algorithms require huge number of simulations depending on the number of decision variables, adjoint optimization method requires only two simulations regardless of the number of decision variables.

The goal of fluid-dynamic design optimization is the maximization (or minimization) of an objective function that is a nonlinear function of a set of discrete flow variables [21]. In design optimization, the question of interest is: what is the perturbation in  $J$  due to a perturbation in the geometry, and hence the flow field? If  $p$  is the perturbation in the flow field, then the linearized perturbation of the function of interest ( $J$ ) is

$$g^T p \equiv \frac{\partial J}{\partial z} p. \quad (15)$$

Therefore, the goal is to evaluate the quantity  $g^T p$  where  $p$  satisfies the appropriate linearized flow equations:

$$Ap = f, \quad (16)$$

where  $A$  is some given matrix. The dual form is to evaluate  $\lambda^T f$  where the adjoint solution  $\lambda$  satisfies the linear system of equations

$$A^T \lambda = g. \quad (17)$$

The equivalence of the two forms can be easily proved as follows:

$$\lambda^T f = \lambda^T Ap = (A^T \lambda)^T p = g^T p. \quad (18)$$

Given a single  $f$  and a single  $g$ , nothing would be gained (or lost) by using the dual form. However, suppose now that we want to value of the objective function for  $k$  different values of  $f$ , and  $n$  different values of  $g$ . The choice would be to do either  $k$  different primal calculations or  $n$  different dual calculations. When the dimension of the system is very large, the cost of the vector dot products is negligible compared to solving the linear systems of equations, and therefore the dual (or adjoint) approach is much cheaper when  $n \ll k$ .

Given a set of design variables  $m$  and a set of flow variables  $z$ , and using the evaluated  $g^T p$ , we can obtain the functional gradient by linearization:

$$\frac{dJ}{dm} = g^T p + \frac{\partial J}{\partial m}, \quad (19)$$

subject to equation (16). Here, the parameters can be defined as:

$$p = \frac{dz}{dm}, \quad A = \frac{\partial F}{\partial z}, \quad g^T = \frac{\partial J}{\partial z}, \quad f = -\frac{\partial F}{\partial m}. \quad (20)$$

The term  $g^T p \equiv \lambda^T f$  can be computed either by the direct approach, solving  $Ap = f$ , or by the adjoint approach, solving  $A^T \lambda = g$ . As said, for a single design variable there would be no benefit in using the adjoint approach, but for multiple design variables, each has a different  $f$ , but the same  $g$ , hence the adjoint approach is computationally much more efficient.

# CHAPTER 3. METHODOLOGY

## 3.1 Numerical model description

An open-source software developed by the applied modelling and computation group in the department of earth science and engineering at Imperial College London was used, named OpenTidalFarm [6]. OpenTidalFarm is capable of simulating and optimizing tidal turbine farms by applying an efficient optimization algorithm onto an accurate flow prediction model. It is worthwhile mentioning that the wakes generated behind the turbines are independent from each other.

### 3.1.1 The design parameters

For the turbine layout optimization problem formulated in 2.4.1, the design parameter  $m$  is a vector containing the positions of each turbines, *Figure 7*.

$$m = \begin{array}{|c|c|c|c|c|c|c|} \hline x_1 & y_1 & x_2 & y_2 & \cdots & x_N & y_N \\ \hline \end{array}$$

*Figure 7*.  $m$  containing design parameters in the turbine layout optimization problem

### 3.1.2 The PDE constraints

In this study, 2-D nonlinear shallow water equations were used as the PDE constraint of the optimization problem. From equation (13), if neglecting the Coriolis force, let drag coefficient expressed with  $c_b$  and  $c_t(m)$  which represent the quadratic bottom friction and the turbine parameterization, respectively, the equation read:

$$\kappa \frac{\partial u}{\partial t} + u \cdot \nabla u - \nu \nabla^2 u + g \nabla \eta + \frac{c_b + c_t(m)}{H} \|u\| u = 0, \quad (21)$$

$$\kappa \frac{\partial u}{\partial t} + \nabla \cdot (Hu) = 0.$$

The parameter  $\kappa \in \{0,1\}$  specifies if the steady ( $\kappa = 0$ ) or the unsteady problem ( $\kappa = 1$ ) is considered; in the unsteady case the time-dependency of the variable definitions above can be neglected.

### 3.1.3 The turbine parameterization

There are several methodologies in terms of the turbine parameterisation, in which actuator disk modeling is known as the most widely used method from wind turbine modeling to the tidal turbine modeling. However, this can be problematic in the context of gradient-based optimization since the friction becomes a non-differential term, hence in this study, a turbine is modeled via an increased bottom friction over a small area [22], a so-called bump function. A bump function in one dimension is:

$$\psi_{p,r}(x) \equiv \begin{cases} e^{1-1/(1-\|\frac{x-p}{r}\|^2)} & \text{for } \|\frac{x-p}{r}\| < 1, \\ 0 & \text{otherwise,} \end{cases} \quad (22)$$

where the two parameters  $p$  and  $r$  are the center and the support radius of the bump function, respectively.

A two-dimensional bump function is obtained by multiplying equation (22) in both dimensions, hence the friction function of a single turbine is :

$$C_i(m)(x, y) \equiv K_i \psi_{x_i,r}(x) \psi_{y_i,r}(y). \quad (23)$$

where it is parameterised by a friction coefficient  $K_i$ .

Finally, the turbine friction function  $c_t$  in the equation (21) is defined to be the

sum of the equation (23) for all  $N$  turbines:

$$c_t(m) \equiv \sum_{i=1}^N C_i(m). \quad (24)$$

### 3.1.4 The functional of interest

A natural choice for the function of interest is the time-averaged power extraction due to the increased friction by the turbines. This follows the same rule with equations (7) - (9), but different in the sense of parameterising the power extraction from turbine.

In the unsteady case ( $\kappa = 1$ ) this is expressed as:

$$J(u, m) = \frac{1}{T} \int_0^T \int_{\Omega} \rho c_t(m) \|u\|^3 dxdt, \quad (25)$$

where  $\rho$  is the fluid density. In the steady condition ( $\kappa = 0$ ) the functional of interest becomes independent from time domain:

$$J(u, m) = \int_{\Omega} \rho c_t(m) \|u\|^3 dxdt, \quad (26)$$

Note that this value represents kinetic power extraction rather than electrical power generation, since it does not incorporate losses due to the turbine support structures and the conversion to electricity.

### 3.1.5 Box and inequality constraints

In the context of the turbine layout optimization problem, a typical condition is to restrict the area in which the turbines may be deployed. In this study, the corresponding sites have rectangular shape, hence box constraints are sufficient to enforce this restriction.

Another common condition is to ensure that individual turbines do not overlap. This is implemented by enforcing a minimum distance  $d_{\min}$  between any two turbines:

$$\|p_i - p_j\|^2 \geq d_{\min}^2 \quad \forall i, j : 1 \leq i < j \leq N. \quad (27)$$

### 3.1.6 Optimization algorithm

A typical gradient-based optimization algorithm was implemented with the following process of iteration:

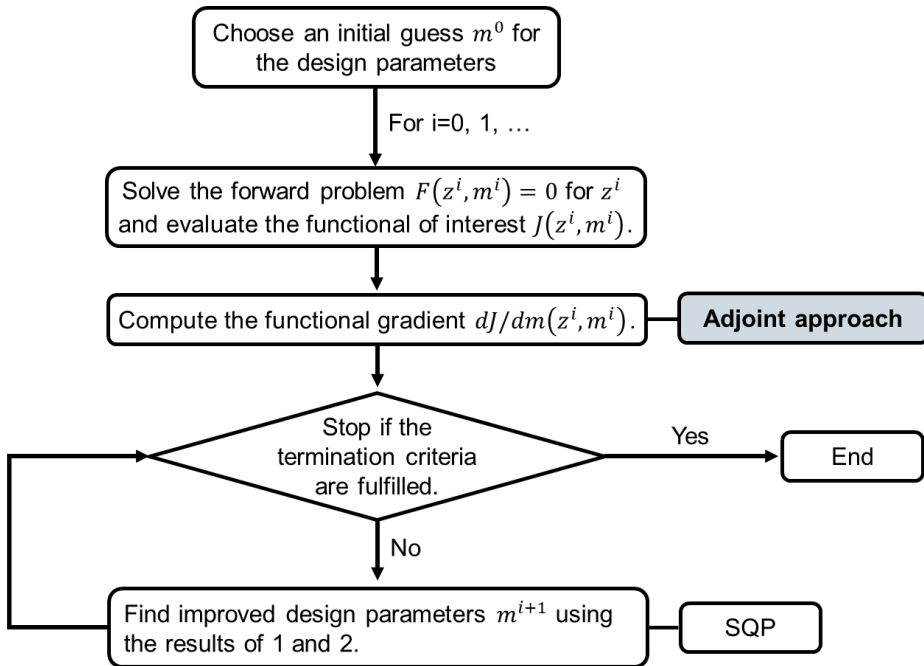


Figure 8. Flow chart of the optimization algorithm

The second step in Figure 8 requires the computation of the functional gradient with respect to the optimization parameters  $dJ/dm$ , which can efficiently be computed using the adjoint method as discussed in 2.4.2.

For the optimization problem considered here, the adjoint shallow water equations driven from equation (19) are:

$$\begin{aligned}
-\frac{\partial \lambda_u}{\partial t} + (\nabla u)^* \lambda_u - (\nabla \cdot u) \lambda_u - u \cdot \nabla \lambda_u - \nu \nabla^2 \lambda_u - H \nabla \lambda_\eta \\
+ \frac{c_b + c_t(m)}{H} \left( \|u\| \lambda_u + \frac{u \cdot \lambda_u}{\|u\|} u \right) = \frac{\partial J^*}{\partial u},
\end{aligned} \tag{28}$$

$$-\frac{\partial \lambda_\eta}{\partial t} - g \nabla \cdot \lambda_u = 0,$$

where  $\lambda \equiv (\lambda_u, \lambda_\eta)$  is the vector containing the adjoint velocity and adjoint free-surface displacement, respectively. Note that the adjoint equations are linear while the forward equations are nonlinear, and therefore solving the adjoint equations is typically much cheaper.

The fourth step was solved using sequential quadratic programming (SQP), which was implemented with the SLSQP algorithm available through the SciPy optimization package.

## 3.2 Experiment overview

### 3.2.1 Experiment procedure

In the following, we present methodology and results for several different layout optimization cases.

First, I'll provide results for standard steady & unsteady flow past a single turbine in order to demonstrate that the flow solver accurately captures tidal turbine wakes, thereby providing confidence that subsequent layout optimizations are performed according to the correct flow physics. Then I'll compare the energy production of a

single turbine under steady & unsteady flow, to find an appropriate comparison condition for the two. The reason why the energy production is the key comparison parameter is because the energy production is the functional of interest (objective) in the relevant optimization algorithm that dominates the optimization procedure.

Second, layout optimization of N-turbine tidal farm using a number of unidirectional constant flow speed have been performed. This experiment was performed in order to demonstrate the insights of the optimized layouts and optimization heuristics of the minimum velocity threshold that enables the optimization to converge to the QGO at a given tolerance. This test was proposed due to the different wake behavior under different flow speed which can cause the difference in the optimization procedure, hence resulting in the different optimized layout. The minimum velocity threshold found in the pilot test will provide a good discussion point for the results of the main test – optimization under the unsteady flow with velocity variations.

Finally, effects of flow unsteadiness in the tidal turbine farm layout optimization procedure compared to the optimization under steady condition have been identified, with regards to the variation in flow speed and direction, respectively. The comparison was performed based on the appropriate comparison condition found in Pilot Test 1. The root cause of the difference in the optimization procedure between the optimization under steady and unsteady, unidirectional flow was identified, which takes account the result from Pilot Test 2 in terms of the flow speed variation. Then, the root cause of the difference in the optimization procedure between the optimization under unidirectional flow and bidirectional flow was identified, to find

the impact of flow direction variation in the optimization procedure. The difference in the result implies that some of the optimization under the flow with unsteadiness might fall into the local optima and cannot converge to QGO. To avoid these situations, a generalized strategy has been suggested in order to make reasonable benefit from the optimization under the flow with unsteadiness and to give an insight of where it can value.

### **3.2.2 Experimental flow chart**

Experimental flow chart is shown in *Figure 9*.

## **3.3 Simulation set-up**

### **3.3.1 Mesh domain**

Several numbers of turbines are to be deployed in a rectangular turbine site of size 320m x 160m. Inside the site area, the mesh was structured with an element size of  $h = 2.5$  m. Outside the site area was constructed with unstructured meshes with a uniform mesh element size of  $h = 10$  m outside the site area. The higher resolution in the turbine site ensures that each individual turbine is well resolved, independent of its location within the site; this obviates the need for re-gridding when the turbines are moved [6]. The resulting meshes consisted of 14084 nodes and 27974 triangles. All meshes were created using Gmsh 2.0.

In all numerical experiments, the optimization algorithm was initialized with the turbines deployed in a regular grid or staggered layout with box constraints for the turbine positions to ensure that the turbines remain inside the site areas.

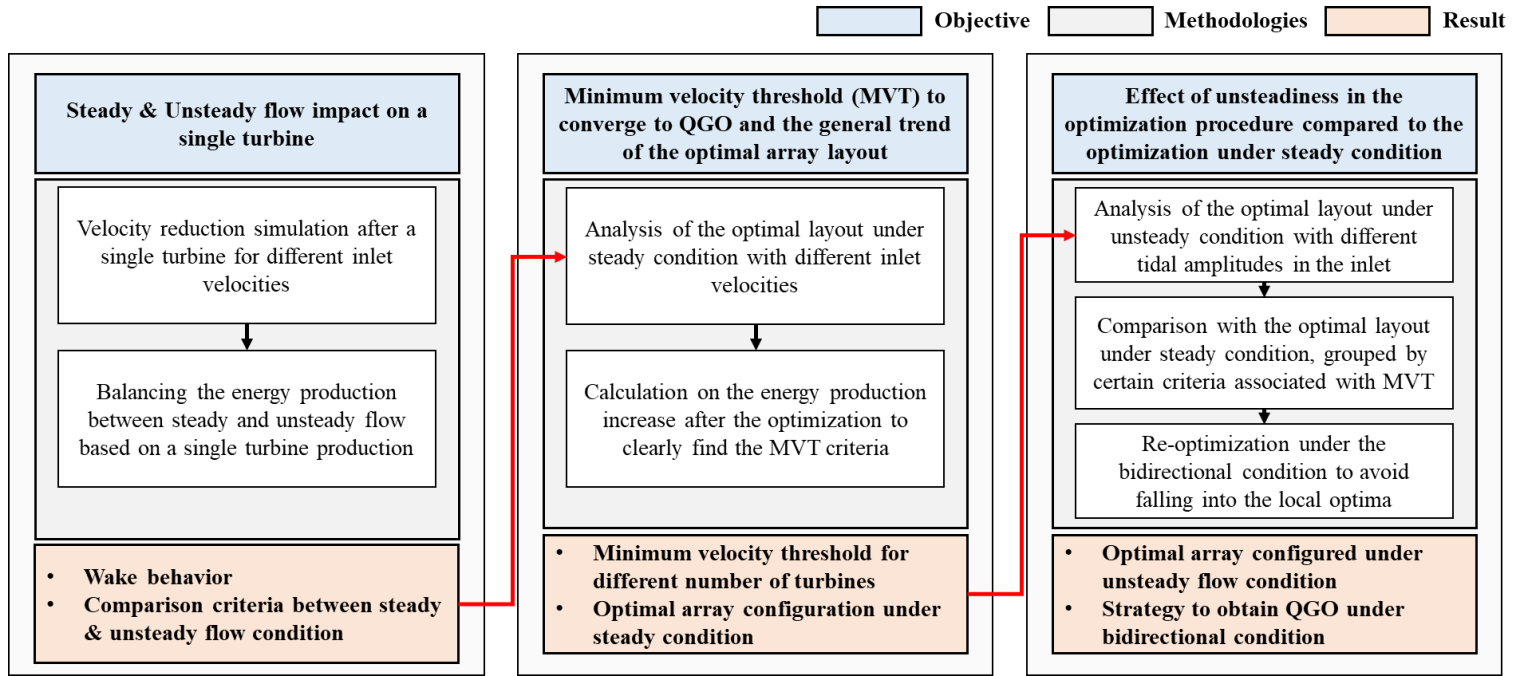


Figure 9. Experimental flow chart

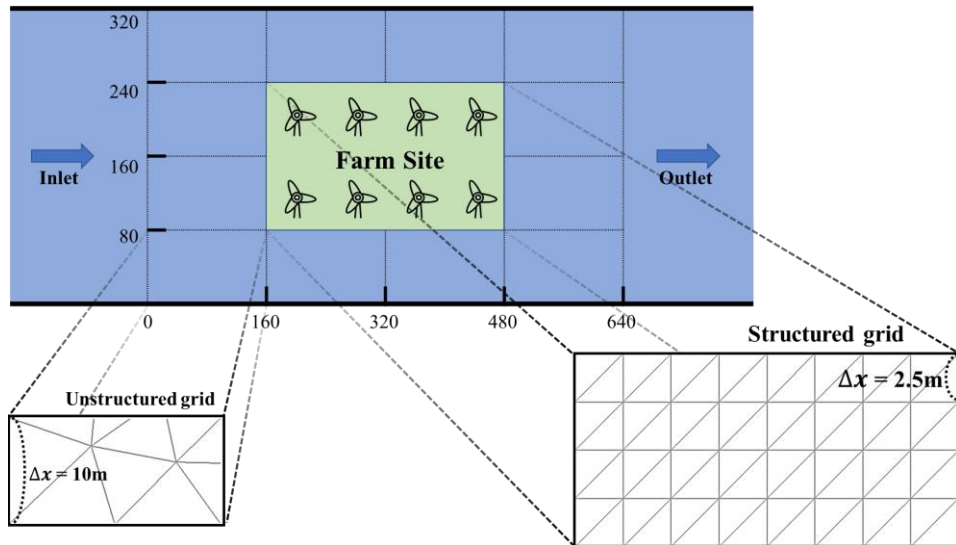


Figure 10. Simulation domain and the grid

### 3.3.2 Boundary condition

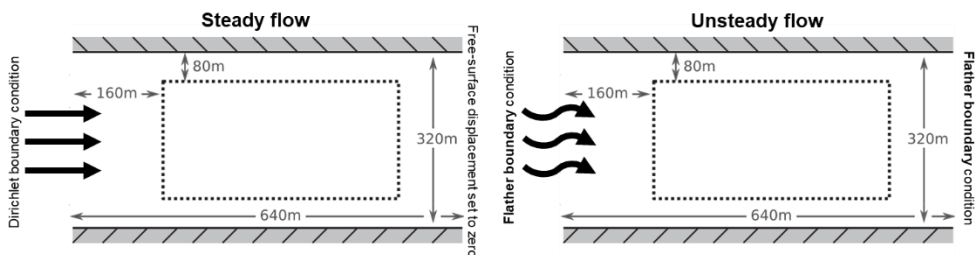


Figure 11. Illustrations of boundary conditions for steady flow (left) and unsteady flow (right) at a given simulation domain

#### i. Steady condition

Steady flow was simulated as a reference for the time-dependent simulations. On the top and bottom boundaries, a free-slip boundary condition was applied and on the outflow boundary, the free-surface displacement was set to zero. On the left boundary

a Dirichlet boundary condition was formulated to enforce a constant velocity. Only the horizontal velocity was enforced, to produce the predominating wake parallel to the channel wall, hence minimize the reflection of the wake that could occur:

$$u_{inlet} = \begin{pmatrix} u_0 \\ 0 \end{pmatrix}, \quad (29)$$

where  $u_0$  is the horizontal inlet velocity.

ii. Unsteady condition

It is not straightforward to describe tidal flows or long waves in a basin using a numerical method. In the conventional problem, the periodic wave-maker generates the incident waves at the open boundaries along with standing periodic wave makers and the numerical sponge is employed to absorb the disturbances from the internal domain. Even though such methods work properly, in 1 or 2D shallow water problem, characteristic method types of open boundary condition seem to have possibility to be proper, if wave celerity are shallowly confined by depth.

Radiation conditions are a popular class of passive OBCs, which are based on the propagation of a quantity through a boundary. One of the extensions of a radiation boundary condition which will be used in this study was originally proposed by Flather [26].

The proper boundary condition should introduce the external information into internal domain and pass or radiate almost disturbances from the internal to out of domains. For the consideration of radiation, the Sommerfeld's equation of wave is introduced as follows:

$$\frac{\partial \psi}{\partial t} + c \frac{\partial \psi}{\partial x} = 0, \quad (30)$$

where  $t$  and  $x$  are time and the coordinate, respectively,  $\psi$  is any physical property that is propagated through a boundary and  $c$  is the characteristic speed of invariants,

$$c = \sqrt{gH}, \quad (31)$$

where  $H$  is water depth and  $g$  is the gravitational acceleration.

For computational reason, the unsteady condition in this study is not a nature condition with spring and neap tides, but a simplified condition with a constant amplitude and period. The simplest possible tidal configuration, a freely propagating sinusoidal long wave in a constant depth channel, is considered. To find a simple equation for the tidal configurations, continuity equation can be rewritten as

$$\frac{\partial \eta}{\partial t} + H \frac{\partial u}{\partial x} = 0, \quad (32)$$

Which gives

$$\frac{\partial}{\partial x} \left[ u - \frac{c}{H} \eta \right] = 0. \quad (33)$$

Finally, integrating across the boundary gives

$$u_{in} = u_{ext} - \sqrt{\frac{g}{H}} (\eta_{in} - \eta_{ext}). \quad (34)$$

The Flather boundary condition can be thought of as applying an adjustment to the externally prescribed normal velocity based on the difference between modeled and externally prescribed surface elevations [26].

Based on equation (34) and equation (6), we can construct the Flather velocity condition in the inlet boundary as,

$$\begin{aligned}
u_{in,horizontal} &= \eta_0 \sqrt{\frac{g}{H}} \cos(-\omega t) - \sqrt{\frac{g}{H}} (-\eta_0 \cos(-\omega t)) \\
&= 2\eta_0 \sqrt{\frac{g}{H}} \cos(-\omega t) = 2\eta_0 \sqrt{\frac{g}{H}} \cos\left(-\frac{2\pi}{T} t\right) \\
&= 2\eta_0 \sqrt{\frac{g}{H}} \cos\left(-\sqrt{gH} \frac{\pi}{L} t\right).
\end{aligned} \tag{35}$$

Therefore, to be more specific it can be described as

$$u_{inlet} = \begin{pmatrix} 2\eta_0 \sqrt{\frac{g}{H}} \cos\left(-\sqrt{gH} \frac{\pi}{L} t\right) \\ 0 \end{pmatrix}. \tag{36}$$

On the top and bottom boundaries, a free-slip boundary condition was applied.

### 3.3.3 Parameter settings

To set the simulation parameters, dimensional analysis should be conducted in advance. A model is a scaled version of the prototype, which enables the efficient analysis of large-scale natural phenomena by reducing their size. When deciding a suitable model dimension, the law of similitude should be considered. Dimensional analysis is a tool useful in analyzing the similarity between a prototype and a model [23].

The primary restoring forces of wave can be either gravity or surface tension based on the wave period [24], and the dynamic similarity between the natural and modeled systems with different scales is satisfied when both systems have identical Froude and Weber numbers. However, since this study is focusing on tidal current which is one of the longest waves, we can disregard the Weber number and consider only the Froude number to examine the dynamic similitude of the model:

$$Fr = \frac{V}{\sqrt{gD}}, \quad (37)$$

where  $V$  is the flow speed,  $D$  is the hydraulic depth,  $g$  is the gravitational acceleration.

The appropriate scale for the model was determined based on these assumptions as the scale wherein the nondimensional numbers of the models were equal to those of the prototype.

As a prototype, one of the tidal turbine farm sites that can be found in Uldolmok, South Korea, was used, where it is well-known with the high flow velocity due to its geographic condition. The Uldolmok Strait experiences peak tidal current speeds of up to 6 m/s with the width of the strait being approximately 300 m, and a water depth of 20 to 32 m below datum level.

*Table 2.* Simulation parameter setting

<b>Parameter</b>	<b>Value</b>
Water depth	$H = 20 \text{ m}$
Viscosity coefficient	$\nu = 3 \text{ m}^2\text{s}^{-1}$
Turbine friction coefficient	$K = 12$
Acceleration due to gravity	$g = 9.81 \text{ m s}^{-2}$
Water density	$\rho = 1000 \text{ kg m}^{-3}$
Bottom friction coefficient	$c_b = 0.0025$
Turbine radius	$r = 10 \text{ m}$
Rotor diameter	$D = 20 \text{ m}$
Minimum distance between any two turbines	$d_{min} = 30 \text{ m}$

The Froude number is the primary measure to evaluate similitude between real nature and model, and the two systems should have a similar Froude number range.

In the prototype of real nature in Uldolmok site, the Froude number results in the range of  $0.34 \sim 0.43$ , with the peak flow speed around  $6 \text{ m/s}$  and the water depth condition:  $20 \text{ m} \leq H \leq 32 \text{ m}$ . In the model, the Froude number results around  $0.2$  at the peak flow speed, hence can be considered to be in a similar number range with the nature property.

The parameters regarding turbine specifications are determined based on the real turbine cases to model the wake structure similar and was set as constant for all the turbines. Minimum distance between any two turbines was enforced to avoid the overlapping during the optimization as in reality.

## **CHAPTER 4. Test cases, Results and Discussions**

### **4.1 Pilot Test 1: Steady & Unsteady flow impact on a single turbine**

First, I'll provide results for standard steady & unsteady flow past a single turbine in order to demonstrate that the flow solver accurately captures tidal turbine wakes, thereby providing confidence that subsequent layout optimizations are performed according to the correct flow physics. The wake effect will be evaluated for different inlet velocities, to demonstrate the reflection of wake effect in the optimization procedure. Then I'll compare the energy production of a single turbine under steady & unsteady flow, to find an appropriate comparison condition for the two.

#### **4.1.1 Wake behavior**

A single turbine pilot case has been generated to estimate the wake behavior under steady flow case and unsteady flow case. Both cases were generated following the boundary condition formulated in 3.3.2. Unsteady flow case was simulated for one tidal period. The turbine was positioned on the centerline of the channel to minimize the wall effect and also to be symmetrical from the wall; *Figure 12 (A)*. Turbine was parameterized with the parameters defined in 3.1.3, with the friction coefficient of 12 and the kinematic viscosity of  $3 \text{ m}^2/\text{s}$ .

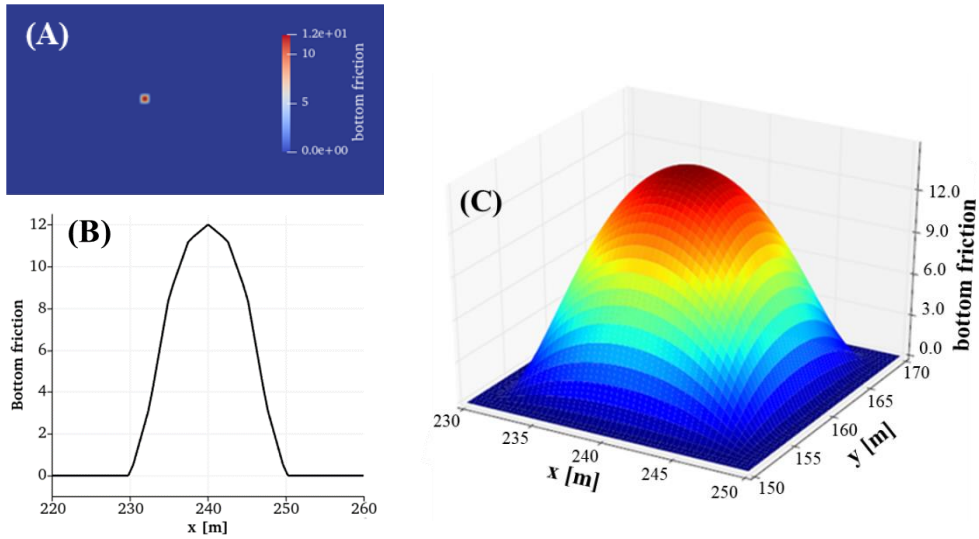


Figure 12. Turbine parameterized with bottom friction when the friction coefficient of 12 and the kinematic viscosity of  $3 \text{ m}^2/\text{s}$ . (A) A bottom friction plot across the channel domain; indicates the single turbine position; (B) 1D:  $\varphi(x|220 \leq x \leq 260, y = 160)$ ; (C) 2D:  $\varphi(x, y|220 \leq x \leq 260, 140 \leq y \leq 180)$

i. Steady condition

Two sample cases with single turbine under different inlet velocities for each are presented to examine the simplest wake behavior. Figure 13 shows the velocity magnitude field and free surface elevation field when a single turbine is deployed under steady flow with  $u_0 = 0.95 \text{ m/s}$  and  $u_0 = 1.56 \text{ m/s}$  from equation (29).

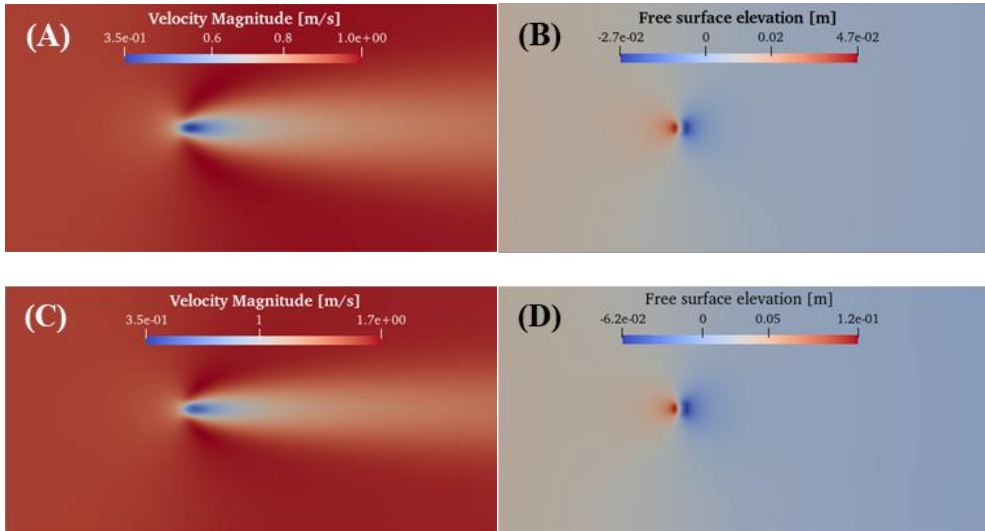


Figure 13. velocity magnitude field (A) and free surface elevation field (B) when a single turbine is deployed under a steady flow with  $\mathbf{u}_0 = 0.95 \text{ m/s}$  from equation (25). Velocity magnitude field (C) and free surface elevation field (D) when a single turbine is deployed under a steady flow with  $\mathbf{u}_0 = 1.56 \text{ m/s}$  from equation (29).

To clearly show the difference in the flow impact after the turbine energy extraction depending on the inlet velocities between the two sample cases, Figure 14 presents the velocity plot along the centerline of the channel for both cases. The quantitative comparison on the turbine energy extraction impact on the flow should be evaluated in accordance with the wake effect, which is defined to be the ratio of velocity reduction after 10 D (rotor diameter) downstream from the turbine position in the current study.

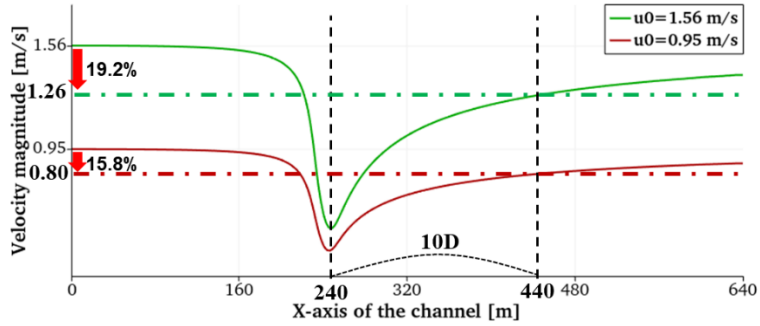


Figure 14. velocity plot along the centerline of the channel when  $u_0 = 0.95 \text{ m/s}$  (red) and  $u_0 = 1.56 \text{ m/s}$  (green) from equation (29). Wake effect resulted in 15.8% reduction when  $u_0 = 0.95 \text{ m/s}$  and 19.2% reduction when  $u_0 = 1.56 \text{ m/s}$ .

Several other wake analyses with different velocities have been performed, resulting with a conclusion that the wake effect tends to get bigger when the inlet velocity increases; Figure 15. This can be applied as a clear reason why the optimized layout under sufficiently high velocity tends to avoid having additional rows, which will be discovered in the Pilot test 2. The measure on the sufficiency will also be evaluated in the Pilot Test 2.

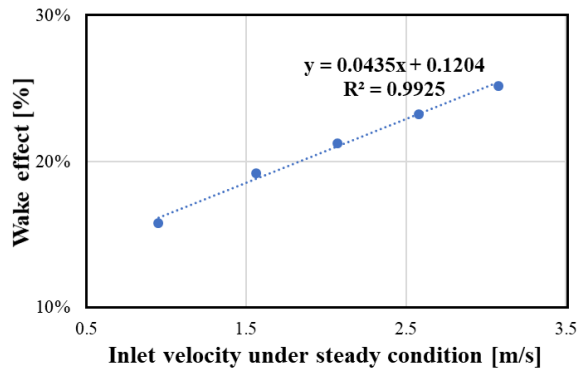
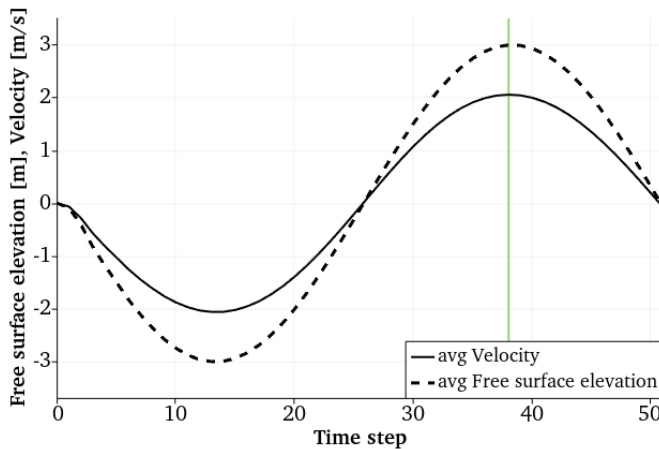


Figure 15. wake effect for 5 different inlet velocities; wake effect tends to get higher when the inlet velocity increases.

ii. Unsteady condition

First, to examine if the unsteady condition is well-developed with the Flather boundary condition formulated in 3.3.2, velocity and free surface elevation over time domain has been simulated across the whole simulation domain; *Figure 16*. A sample unsteady flow case with  $\eta_0 = 1.8 \text{ m}$  from equation (36) has been generated, which clearly shows that the two parameters are moving in-phase with  $\sqrt{gH^{-1}}$  ( $= 0.7$  with the simulation parameters defined in 3.3.3) scale difference in terms of the magnitude, hence is aligned with what we have derived in equation (6).



*Figure 16.* average velocity and average free surface elevation plot over time domain under an unsteady flow with  $\eta_0 = 1.8 \text{ m}$  from equation (36).

We can then evaluate the wake effect under unsteady flow case. *Figure 17* captures the velocity field during one tidal period in a pre-defined bidirectional tidal flow. Wake behavior found to be moving around depending on the flow direction under the bidirectional flow. Only the horizontal velocity was considered in this study to simplify the problem, hence the wake is only moving in two directions.

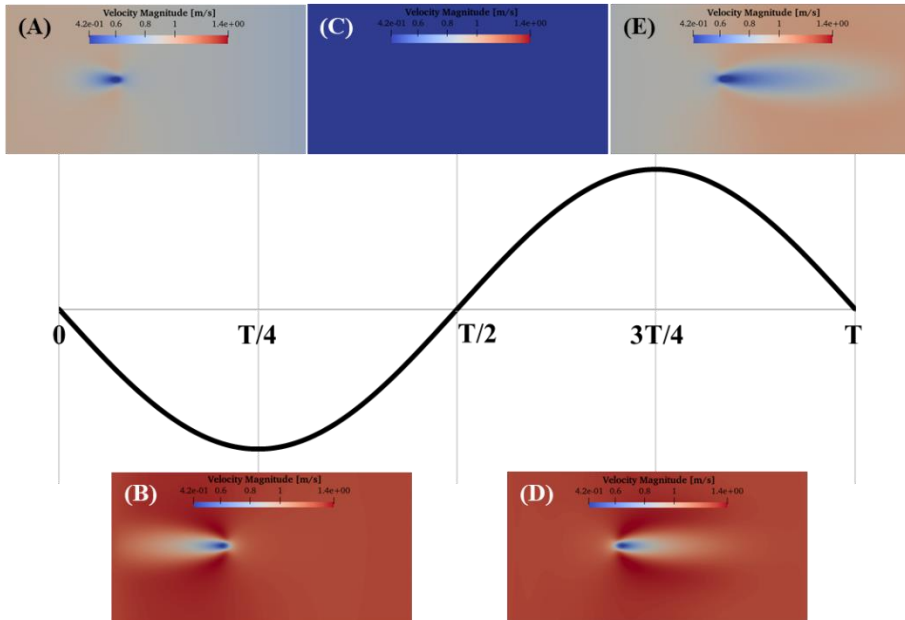


Figure 17. velocity magnitude field when a single turbine is deployed under an unsteady flow with  $\eta_0 = 1.8 \text{ m}$  from equation (36); each figure captured after (A)  $T/8$ , (B)  $T/4$ , (C)  $T/2$ , (D)  $3T/4$ , and (E)  $7T/8$  since the flow has started.

The velocity plot along the channel at different time frame is shown in *Figure 18*, and the wake effect (ratio of velocity reduction after 10 D (rotor diameter) downstream from the turbine position) with regards to the inlet velocities which differs according to the time is plotted in *Figure 19*. It is worthwhile mentioning that within a tidal cycle under unsteady flow condition, the wake effect tends to get smaller when the inlet velocity increases.

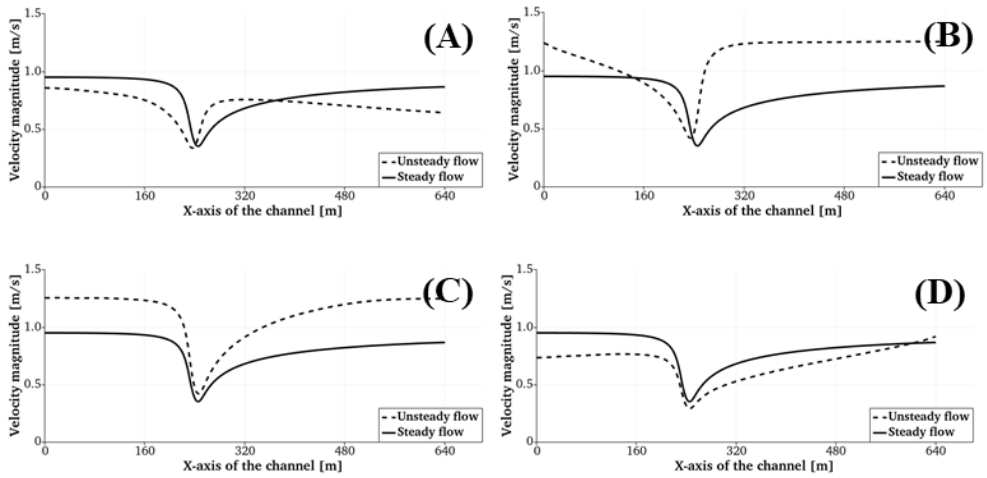


Figure 18. velocity plot along the centerline of the channel after (A)  $T/8$ , (B)  $T/4$ , (C)  $3T/4$ , and (D)  $7T/8$  since the flow has started.

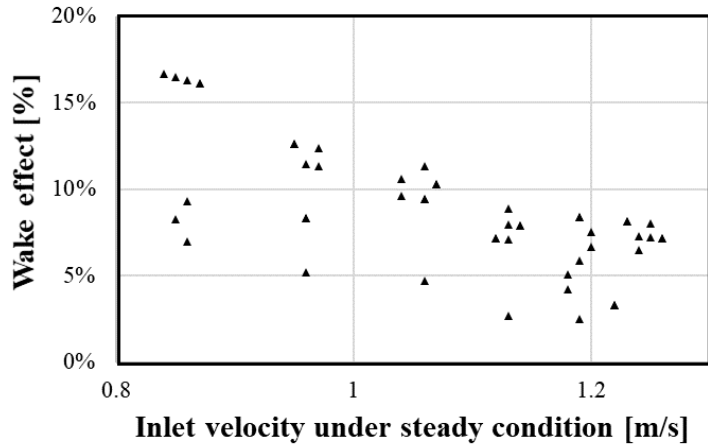
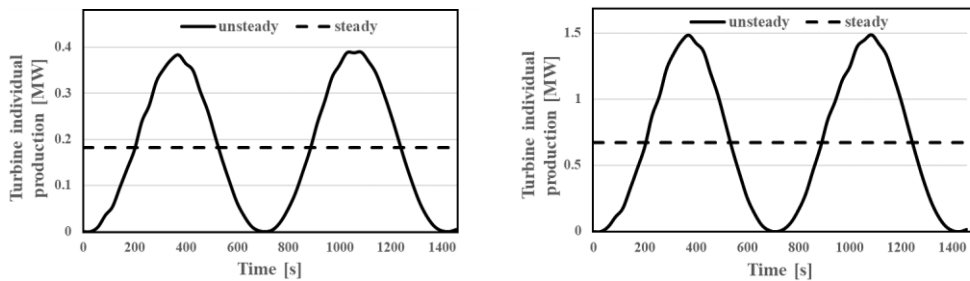


Figure 19. wake effect with regards to the inlet velocities, which differ by each time step when a single turbine is deployed under an unsteady flow with  $\eta_0 = 1.8 \text{ m}$  from equation (36).

#### 4.1.2 comparison criterion between steady and unsteady flow based on the energy production

A single turbine pilot case has been generated to compare the energy production between a steady flow case and unsteady flow case. The reason why the energy production is the key comparison parameter is because the energy production is the functional of interest in the relevant optimization algorithm that dominates the optimization procedure.

It is important to note that energy production in an unsteady flow should differ according to the differences in the flow speed during the flow, hence the comparison will be based on the averaged energy production over the flow cycle. *Figure 20* is showing the energy production plot over tidal cycle as an example of the difference.



*Figure 20.* difference in the energy production between the unsteady sinusoidal flow with maximum velocity of 1.3 m/s and the steady flow with 0.95 m/s velocity. A cyclic-averaged single turbine production was equal in both condition with 0.18 MW (left); Difference in the energy production between the unsteady sinusoidal flow with maximum velocity of 2.1 m/s and the steady flow with 1.56 m/s velocity. A cyclic-averaged single turbine production was equal in both condition with 0.67 MW (right).

Therefore, the comparison will be considered only when equation (38) are set to have a same value for each case, which means when the cyclic-averaged water power of unsteady flow is equal to that of the steady flow. This is to assure that the  $c_p$  for the two cases can be compared to the same available power from the water.

$$J_{unsteady}(u, m) = \frac{1}{T} \int_0^T \int_{\Omega} \rho c_t(m) \|u\|^3 dx dt, \quad (38)$$

$$J_{steady}(u, m) = \int_{\Omega} \rho c_t(m) \|u\|^3 dx dt,$$

As of a simple comparison criterion, the relationship between the inlet velocities has been found, which is easy to implement when enforcing boundary conditions as defined in 3.3.2, hence will make the experiment much easier when constructing many test cases.

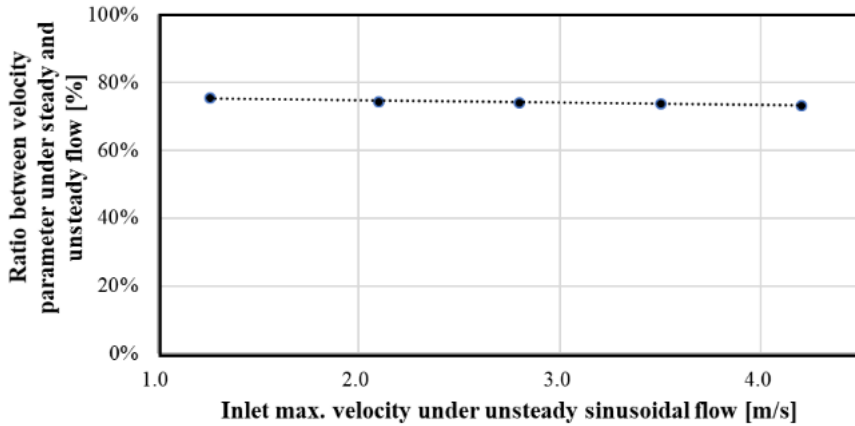


Figure 21. relationship between steady velocity and unsteady maximum velocity when the energy production is the same over a tidal period.

*Figure 21* is indicating that a cyclic-averaged single turbine production under unsteady sinusoidal flow with maximum velocity of  $u_{max}$  is equal to the instant single turbine production under steady flow with approximately  $0.74 u_{max}$ .

#### **4.1.3 Conclusion of Pilot test 1**

- Key take-aways from wake analysis under steady condition
  - Wake effect tends to get bigger when the velocity increases.
  - This can be applied as a clear reason why the optimized layout under sufficiently high velocity tends to avoid having additional rows, which will be discovered in the Pilot test 2. The measure on the sufficiency will also be evaluated in the Pilot Test 2.
  
- Key take-aways from wake analysis under unsteady condition
  - Unsteady flow generated in the study is well-developed with the Flather boundary condition as we have expected.
  - Wake direction tends to move horizontally depending on the flow direction under the bidirectional flow.
  - Within a tidal cycle, the wake effect tends to get smaller when the inlet velocity increases.
  
- Key take-aways from comparison criterion test between steady vs unsteady
  - Cyclic-averaged single turbine production under unsteady sinusoidal flow with maximum velocity of  $u_{max}$  is equal to the instant single turbine production under steady flow with approximately  $0.74 u_{max}$ .

## **4.2 Pilot Test 2: Minimum velocity threshold (MVT) to converge to QGO and the concept of the optimized layout**

Second, layout optimization of N-turbine tidal farm using a number of unidirectional constant flow speed have been performed. This experiment was performed in order to demonstrate the insights of the optimized layouts and optimization heuristics of the minimum velocity threshold (MVT) that enables the optimization to converge to the QGO at a given tolerance. This test was proposed due to the different wake behavior under different flow speed which can cause the difference in the optimization procedure, hence resulting in the different optimized layout. The MVT found in the pilot test will provide a good discussion point for the results of the main test – optimization under the unsteady flow with velocity variations.

### **4.2.1 Test cases**

Since the aim of this test is to find MVT at a stable wake generation condition, only the steady flow conditions were generated following the boundary condition formulated in 3.3.2.

The optimized layouts and the MVT should differ depending on the number of turbines that are to be deployed in the subsequent farm site, hence the study was performed for a set of different number of turbines.

Non-dimensional parameter  $E$  has been introduced, to determine the appropriate number of turbines that can derive a meaningful result.  $E$  represents the ratio of the total length of a linear fence composed of N turbines with an intra-spacing of  $d_{min}$

and a turbine diameter of  $D$  to the lateral width of the farm site,  $L_Y$ ; equation (39). When  $E > 1$ , the layout cannot exhibit a linear configuration with the given constraints. When  $E \leq 1$ , the solution converged to a linear fence, regardless of the convexity of the initial layout [8].

$$E = \frac{(N - 1)d_{min} + D}{L_Y} \quad (39)$$

As said, it is obvious when  $E \leq 1$ , that the solution converges to a linear fence. Therefore, only the maximum number of turbines that still makes  $E$  below 1 was decided to be the smallest number of turbines to be used in the present Pilot test, which is  $N = 5$ . This results in  $E = 0.875$ .  $N = 5$  case will be used as the simplest test case, to reassure that the solution converges to a linear fence.

We'll then slowly increase the number of turbines, until it reaches  $N = 9$  because the array breakdown starts to occur from  $N = 9$ . When excess turbines are deployed to the domain, the array starts to break apart, and a few turbines become detached from the main body. The detached turbines were then placed upstream by an appropriate distance where the wake of the separated turbine diffuses, helping the turbine in the downstream avoid the negative impact of wake on the power production [8].

The previous study found the importance of the initial layout in the optimization procedure. It has stated that the initial layout is critical for the gradient-based algorithm to overcome its inherent limitation of convergence to local optima and to ensure the convergence to QGO at a low computational cost [8]. Therefore, to remove the bias, regular grid/stagger layout was used as the initial layout.

Based on these settings, optimization under steady flow with different  $u_0$  from equation (29) was performed for each number of turbines.  $u_0$  was slowly increased from 1.0 m/s with a step of 0.1 m/s, to find when it converges to a QGO.

#### 4.2.2 Finding minimum threshold of velocity (MVT)

The MVT to converge to QGO has been analyzed for several different cases to support the discussion on the effect of unsteadiness in the optimization procedure.

*Figure 22* is showing some representative cases that helps understanding the optimization procedure and the heuristics of MVT. The optimized layouts with box around are the from optimization under smallest  $u_0$  that enables the convergence to QGO, hence indicating the MVT.

There are two important conditions found when defining MVT:

- i. The velocity when the turbines start to converge in a one-body array.
- ii. The velocity when the total energy production has increased dramatically compared to the previous production increase step.

From  $N = 5 \sim 8$ , condition (i) and (ii) lead to the same conclusion; *Figure 22* and *Figure 23*. *Figure 23* is showing the production plot along the optimization iteration step, for different flow speeds, for each different number of turbines. The red lines are indicating optimization iteration procedure under MVT, which have very clear jumping point compared to the lines below (optimization iteration procedure under the velocity lower than MVT). Energy production is within log-scale in *Figure 23*, because the energy production is in cubic-scale for each velocity, equation (38),

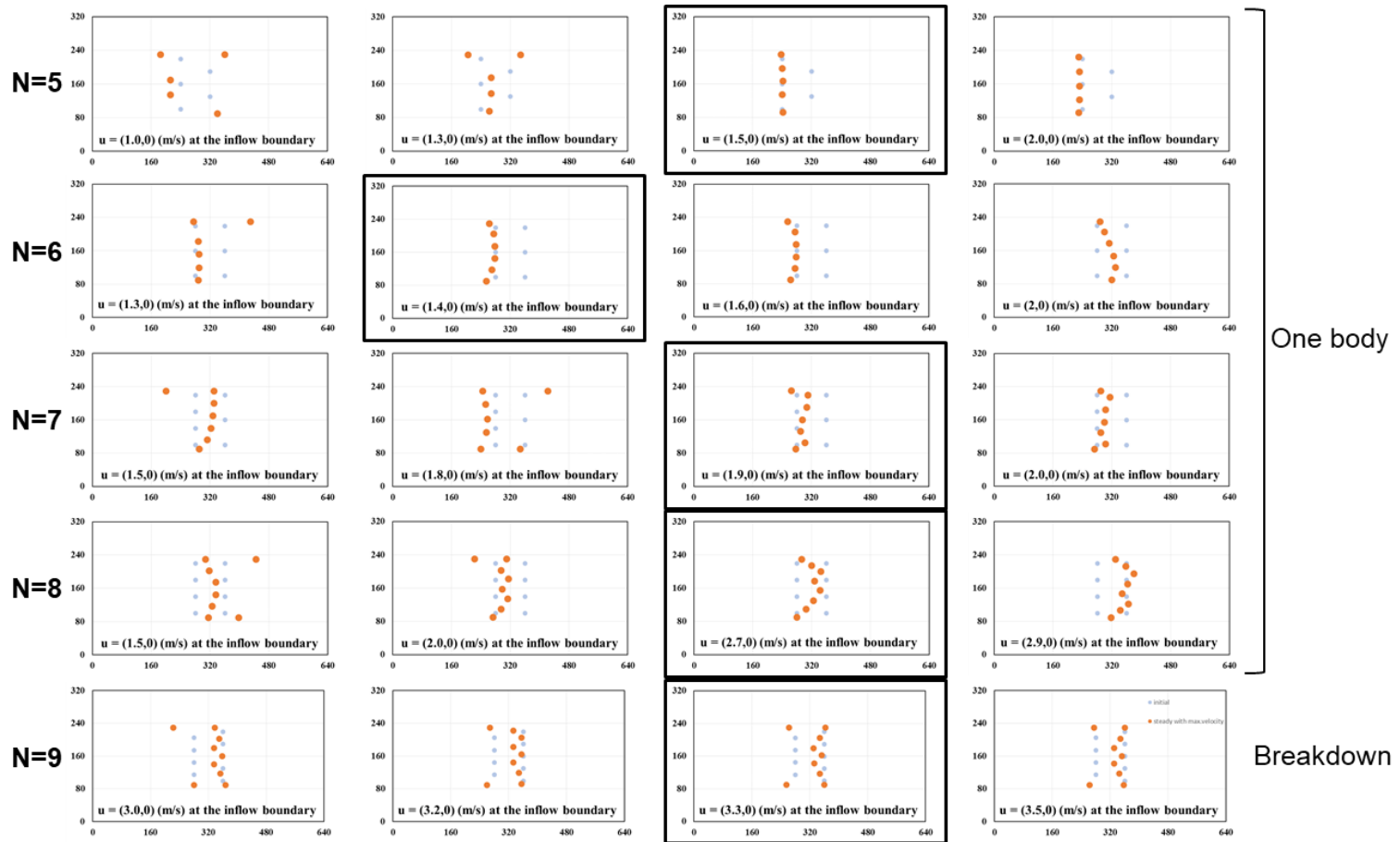


Figure 22. optimized layout under the steady flow condition with different  $\mathbf{u}_0$  from equation (29) for different number of turbines

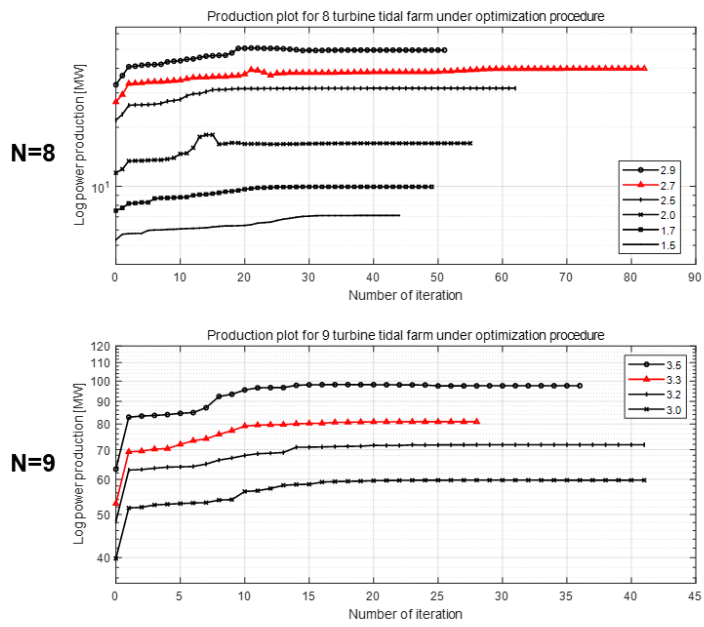
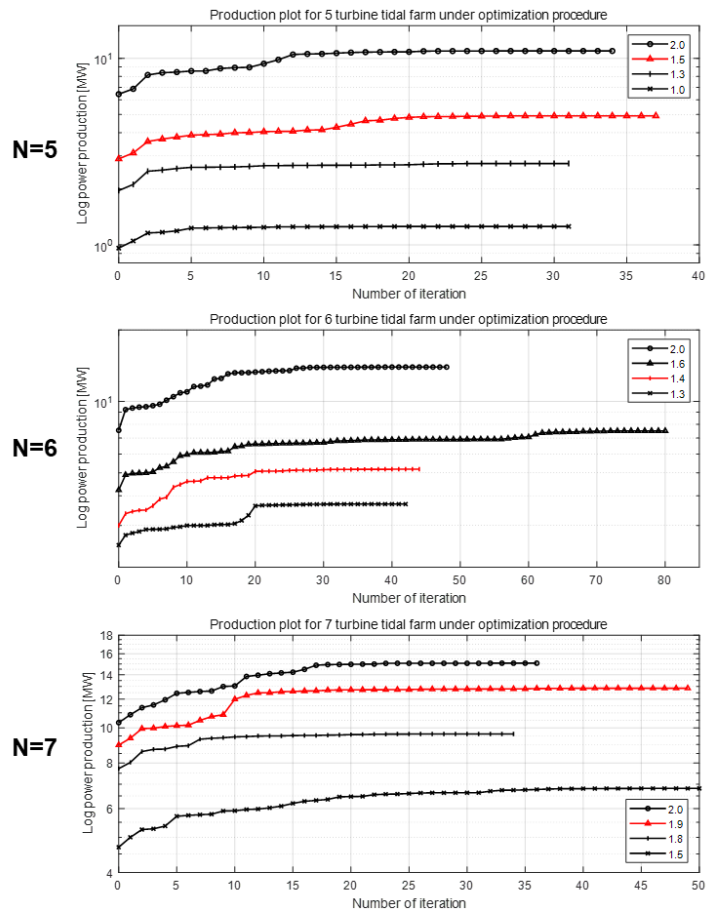
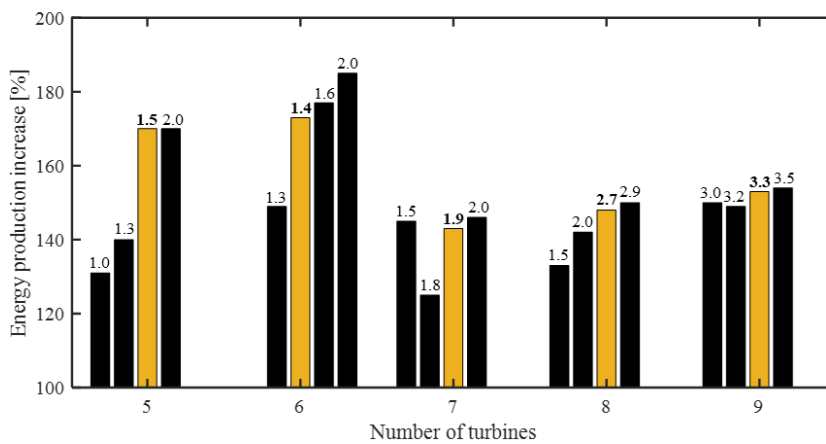


Figure 23. production plot along the optimization procedure, for different flow speeds, for each different number of turbines

which makes the production difference between velocities too huge to be plotted and identified in one graph. *Figure 24* is showing the power production increase, compared to the production under initial layout, again showing how much the production increases after the optimization and when the production has increased dramatically.



*Figure 24.* power production increase, compared to the production under initial layout; production increase for MVT is indicated in yellow and the corresponding velocities are on the top of the bar

For  $N = 9$ , optimal array already started to break down from when there is a small flow speed enforced, hence no dramatic change in the layout concept or dramatic increase in the energy production was found when reaching the MVT. However, the optimized layout became symmetric about the x-axis when the velocity reaches 3.3 m/s, and then continues to keep the similar array shape under higher velocities, which makes 3.3 m/s sufficient to be confirmed as MVT when  $N = 9$ . Therefore, we can

add two more minor conditions when it is hard to configure the two major conditions, (i) and (ii), when defining MVT:

- iii. The velocity when the turbines exhibits symmetric array about the x-axis.
- iv. The velocity when the array starts & continues to keep the similar array shape when increasing the enforcing velocity.

The resulting MVT for each number of turbines are shown in *Table 3*.

*Table 3*. Minimum threshold of velocity to converge to QGO

Number of turbines	E	Minimum threshold of velocity [m/s]
5	0.875	1.5
6	1.0625	1.4
7	1.25	1.9
8	1.4375	2.7
9	1.625	3.3

### 4.2.3 Insights on the optimized layout

Based on the findings from 4.2.2, *Figure 25* is showing some representative cases that helps understanding the optimization heuristics. The representative cases are with sufficient velocity (higher than MVT) forced in the inlet, to assure that the presented layouts can be assumed as QGOs.

It was found that the solution eventually converges to linear fence when  $N = 5$ . This is re-verifying the previous study that the solution converges to a linear fence when  $E \leq 1$ . From  $E > 1$ , the layout cannot exhibit a linear configuration with the

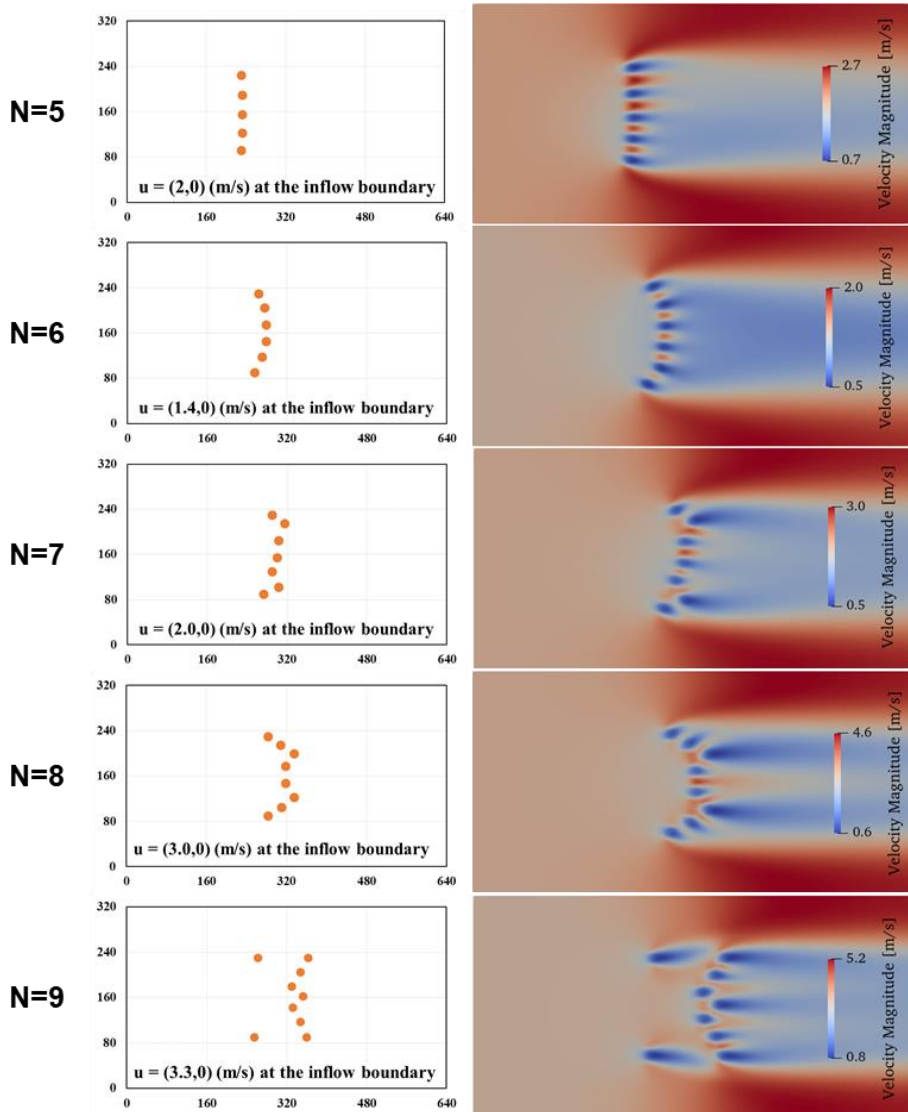
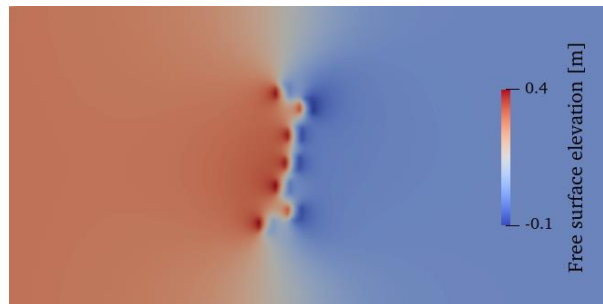


Figure 25. Optimal layout (QGO) and the velocity contour for each number of turbines

given constraints. The optimal layout was developed into an arc-shaped fence when  $N = 6$ . When  $N = 7$ , instead of the increase in the curvature of the array, the optimal array exhibited rather sophisticated barrier.  $N = 8$  possess a M-shape layout to the

downstream and finally we can find that turbines are detached from the array and the array breaks into two parts when  $N = 9$ . It is worthwhile noting that the main body in the optimal layout of  $N = 9$  is having a V-shape layout. It is also worthwhile noting that the turbines tend to curve towards where the flow is coming from, except for when  $N = 9$ , where the two detached turbines already found a position in the upstream. Two turbines are separated from the main body and placed as close as possible to the wall in the north and south, to reduce the wake impact to the main body as much as possible. The main body itself, within the same methodology to reduce the wake impact, tries to maintain a structure where it is curved to the downstream and keeps the body relatively heavy in the center.

Overall, the cluster of turbines exhibit huge wake loss in the downstream, which also yields some elevation difference across the tidal farm, *Figure 26*.



*Figure 26.* Free surface elevation contour for the optimal layout of  $N = 7$  case

#### 4.2.4 Conclusion of Pilot test 2

- Key take-aways from minimum threshold of velocity (MVT) study
  - MVT can be configured following 4 criterions, in the order of consideration weight:



### **4.3 Main test: Effect of unsteadiness in the optimization procedure compared to the steady condition**

Finally, effects of flow unsteadiness in the tidal turbine farm layout optimization procedure compared to the optimization under steady condition have been identified, with regards to the variation in flow speed and direction, respectively. The comparison was performed based on the appropriate comparison condition found in Pilot Test 1. The root cause of the difference in the optimization procedure between the optimization under steady and unsteady, unidirectional flow was identified, which takes account the result from Pilot Test 2 in terms of the flow speed variation. Then, the root cause of the difference in the optimization procedure between the optimization under unidirectional flow and bidirectional flow was identified, to find the impact of flow variation in the optimization procedure. The difference in the result implies that some of the optimization fell into the local optima and did not converge to global optima. To avoid these situations, a generalized strategy has been suggested in order to make reasonable benefit from the optimization under the flow with unsteadiness and to give an insight of where it can value.

#### **4.3.1 Test cases**

Optimizations were performed for several cases for both steady flow and unsteady flow. Both cases were generated following the boundary condition formulated in 3.3.2. Each unsteady flow cases were simulated for 5 tidal period to remove the impact of initial forcing in the flow. The turbines were initially positioned in a same initial layout with that of Pilot test 2, for the comparison reason.

Since the case with  $N = 5$  is rather simple and symmetric from north-to-south and west-to-east when optimized – linear fence, it should not make a recognizable difference in terms of the optimization with directional and magnitude-wise variation, hence the  $N = 5$  case was disregarded in the main test. Cases with  $N = 6 \sim 9$  turbines were considered, for a few different tidal amplitudes.

Optimization under unsteady flow with different  $\eta_0$  from equation (36) was performed for each number of turbines. I have slowly increased  $\eta_0$  from 2.0 m with a step of 0.5 m until 6.5 m, when it was enough to obtain all the cases that could derive a good discussion. Every optimization simulation under unsteady flow were compared with each optimization simulations under steady flow based on the comparison criteria that was found in Pilot test 1.

The test cases were then divided into certain groups according to the maximum velocity that it was simulated. Before defining the criteria for grouping, let's define

$$u_{max} = \sqrt{\frac{g}{H}}\eta_0 \cong 0.7\eta_0, \quad (40)$$

where  $u_{max}$  is the maximum velocity in the peak sinusoidal flow within unsteady flow. We found in Pilot test 1 that the cyclic-averaged single turbine production under unsteady sinusoidal flow with maximum velocity of  $u_{max}$  is equal to the instant single turbine production under steady flow with approximately  $0.74u_{max}$ . Let's define this as,

$$u_{steady,p} \cong 0.74u_{max} \cong 0.52\eta_0. \quad (41)$$

The velocities in the test cases are grouped based on this finding:

For each number of turbines,

- i.  $u_{max} < MVT$   
: when none of the velocities during the optimization exceed MVT
- ii.  $u_{steady,p} \cong 0.74u_{max} < MVT, u_{max} > MVT \rightarrow MVT < u_{max} < \frac{MVT}{0.74}$   
: when the peak velocity exceeds MVT, but not the  $u_{steady,p}$
- iii.  $u_{steady,p} \cong 0.74u_{max} > MVT \rightarrow u_{max} > \frac{MVT}{0.74}$   
: when the  $u_{steady,p}$  exceeds MVT

For each  $u_{max}$ , the test cases are consisted of 3 sets of optimization simulations with different flow conditions for each:

- i. unsteady, bidirectional flow with maximum velocity of  $u_{max}$
- ii. unsteady, unidirectional flow with maximum velocity of  $u_{max}$
- iii. steady flow with velocity of  $u_{steady,p}$

The comparison between the optimal layout under steady condition and the optimal layout under unidirectional but unsteady condition will give an insight on the impact of flow velocity magnitude unsteadiness on the layout optimization procedure.

The comparison between the optimal layout under steady/unidirectional condition and the optimal layout under bidirectional condition will give an insight on the impact of flow directional unsteadiness on the layout optimization procedure.

The results are presented with the time-averaged production to configure the most optimized layout.

### 4.3.2 Optimal layout for each flow conditions

From approximately 120 test cases, including both steady and unsteady flow conditions, *Figure 27* and *Figure 28* are showing some of the major resulting optimal layouts from simulations.  $\eta_0$  and  $u_{max}$  are the enforced parameters for unsteady flow conditions and  $u_{steady,p}$  is the corresponding velocity for steady flow condition. The blue field is indicating when  $u_{max} < MVT$ , the yellow field is indicating when  $MVT < u_{max} < \frac{MVT}{0.74}$ , and the green field is indicating when  $u_{max} > \frac{MVT}{0.74}$ .

The first impression is that even though the optimizations were performed from the same initial condition and same power production for each number of turbines in the beginning, they have all resulted very differently depending on which flow conditions were enforced during the optimization. Among the simulations, certain optimization procedures can fall into local optima, and some can end up with a convergence to QGO.

Therefore, I'll illustrate if the layout optimization under 3 main flow conditions converge to QGO for each subsequent flow conditions, and if not, how to derive a QGO for certain flow conditions. The strategy to derive QGO and the relevant QGO itself will also be suggested in 4.3.3 and 4.3.4.

Before going into the analysis of the optimal layout, let's touch on the definition of the layout similarity that will be continuously discussed in the main test.

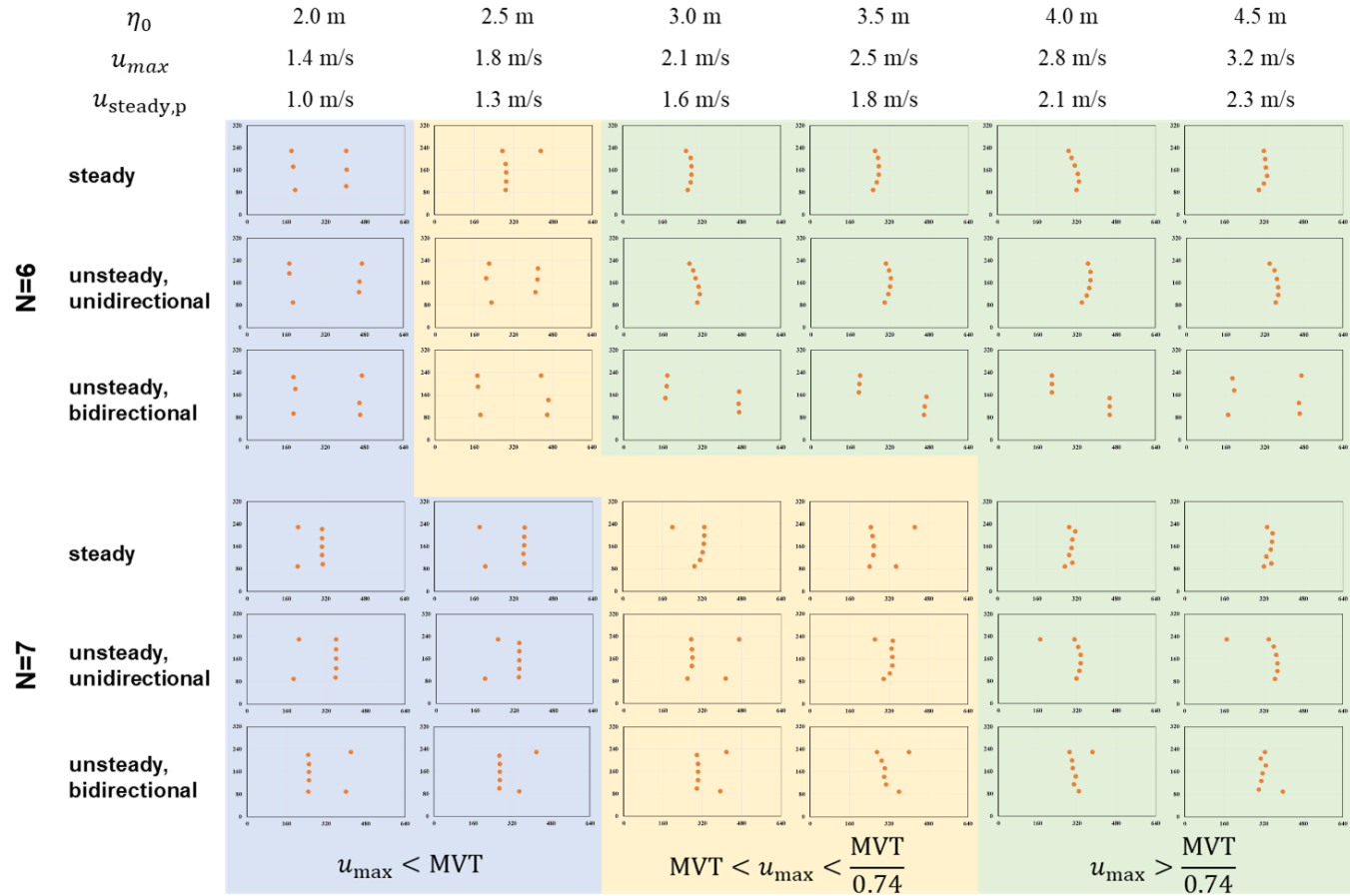


Figure 27. layout optimization for different flow conditions when  $N = 6$  and  $N = 7$

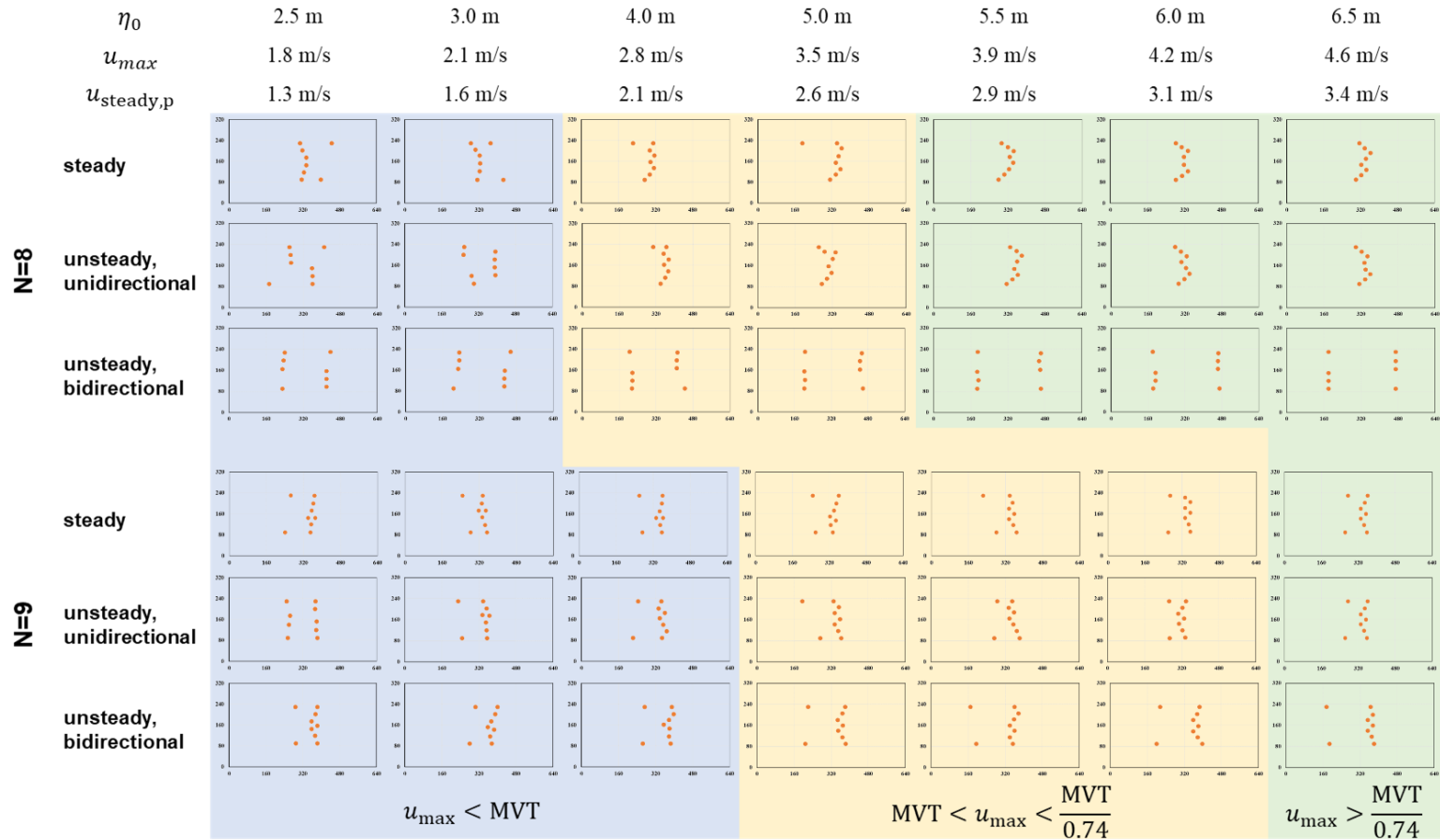


Figure 28. layout optimization for different flow conditions when  $N = 8$  and  $N = 9$

The criteria for the layout similarity can be:

- i. the distribution of the turbines – if it is one-body or not, how many turbines are detached from the main body, how many rows, etc.
- ii. the shape of the main body – linear, arc, V-shape, M-shape
- iii. the placement of the detached turbines – upstream and downstream
- iv. the curvature direction

If the two different arrays are satisfying to be similar within these criteria, we define that the arrays are similar to each other. None of the arrays are exactly the same due to small differences in the optimization procedure, however since we are only identifying QGO not the true global optima, we can consider that the similar array shape is enough to be considered as having same QGO.

First, the optimal layout heuristics under the steady flow condition has already been configured in the Pilot test 2 that it tends to structure one-body array when the velocity increases and finally converge to one-body array (QGO) when the enforced velocity is higher than MVT.

Second, the optimal layout under the unidirectional flow condition was found to have similar array shape with the optimal layout that was found under steady condition when  $u_{max} > \frac{MVT}{0.74}$ . There found exceptional cases for this theory when  $N = 7$ . It tends to exhibit a very different optimal layout in between when  $MVT < u_{max} < \frac{MVT}{0.74}$ , due to the impact of  $u_{max}$  exceeding MVT at a certain point during the sinusoidal velocity profile. Since the energy production is in cubic-scale for each

velocity, equation (38), it is likely that the high velocity in the peak has driven the optimization procedure.

In short, the optimal layout under unidirectional flow condition is similar to the optimal layout under steady condition when it satisfies the velocity condition  $u_{max} > \frac{MVT}{0.74}$ . This implies that the MVT to converge to QGO can be applied in the same way to the unidirectional flow.

Lastly, for the bidirectional flow condition, the optimal layout is different from the ones that we have found for the previous flow conditions where the direction of the flow was always the same. *Figure 29* is showing the tidal farm production under the bidirectional flow condition for layouts optimized under different flow conditions when  $\eta_0 = 4$  m and  $N = 7$ . When we have more detailed look into the peak of the cycle, we can easily find that the layouts optimized under steady and unidirectional flow conditions are showing more production when the flow direction is positive, but the layout optimized under bidirectional flow condition is much more productive when the flow direction is negative. This is because the optimization under bidirectional flow condition have to consider the wake effect generated from both directions, which means it has to consider the balance between the production in each direction. *Figure 30* is showing a velocity magnitude contour in both direction for each optimal layout as an example.

However, the optimization under bidirectional flow condition found to have a high risk that can easily fall into the local optima - optimal layouts under bidirectional flow when  $N = 6$  and  $N = 8$ , which led to 20% and 15% reduction in the energy

production respectively, compared to the QGO found under steady condition. This can easily be observed from the very first step of the optimization iteration, *Figure 31*, where the turbines are separated into two groups to move far away from each other due to the SLSQP algorithm under the process. This is generally a good strategy to reduce the wake impact from each other, but cannot serve as a QGO because of what we have found in Pilot test 2. There it strongly implies that it is much more productive to cluster into one-body to construct a barrier rather than to be separated, unless the number of turbines is kept below 9 where it is almost impossible to cluster into one-body array. It is clearly shown in *Figure 32* that the production of the layout optimized under bidirectional flow condition is way behind the production of the layout optimized under unidirectional flow conditions when  $N = 6$  and  $N = 8$ .

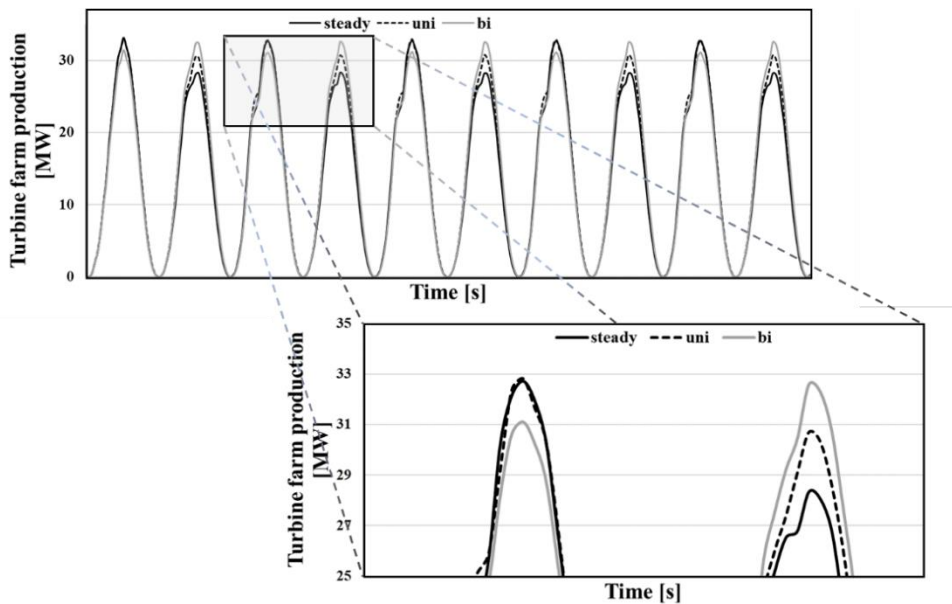


*Figure 29.* tidal farm production under the bidirectional flow condition for layouts optimized under different flow conditions when  $\eta_0 = 4$  m and  $N = 7$

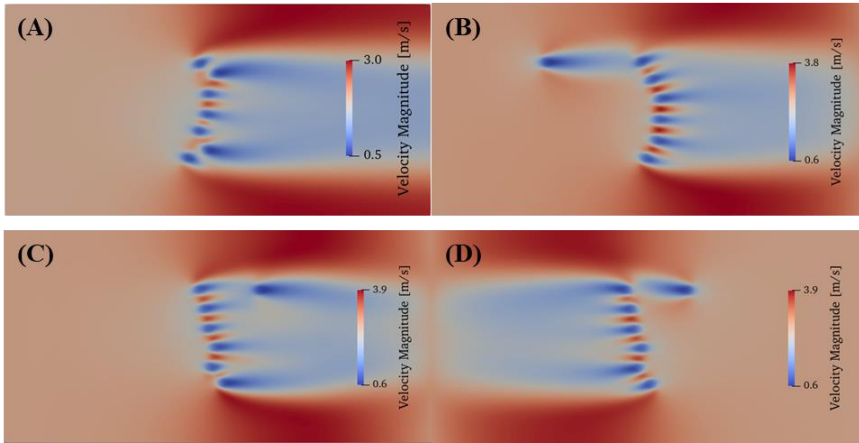


Figure 30. velocity magnitude contour for each layout optimized under three different flow conditions when  $\eta_0 = 4$  m and  $N = 7$ ; (A) steady flow, (B) unsteady, unidirectional flow, (C) unsteady, bidirectional flow at the highest velocity peak in positive direction and (D) at the highest velocity peak in negative direction

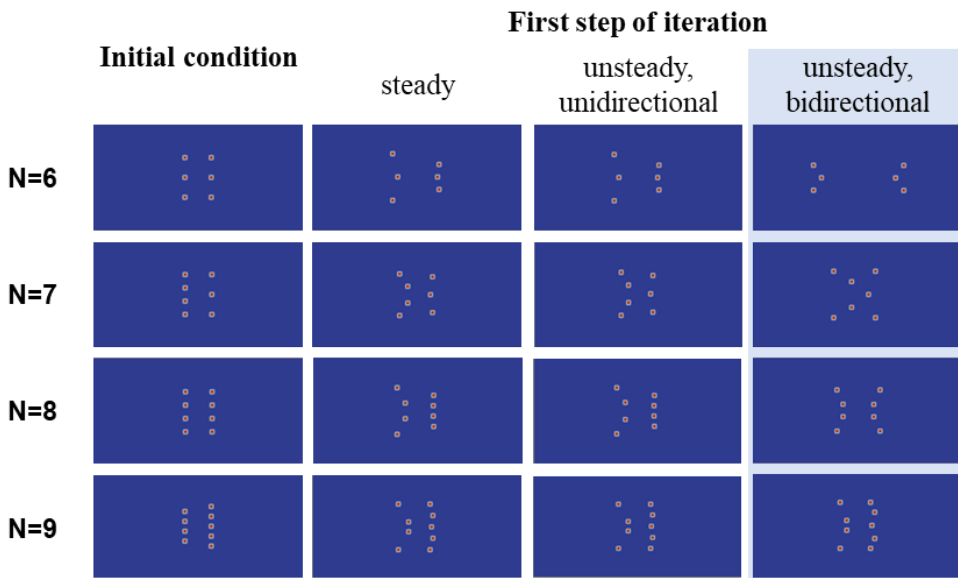


Figure 31. Difference in the first step of optimization for each flow conditions when  $\eta_0 = 4$  m; it is clearly very much different under the bidirectional flow

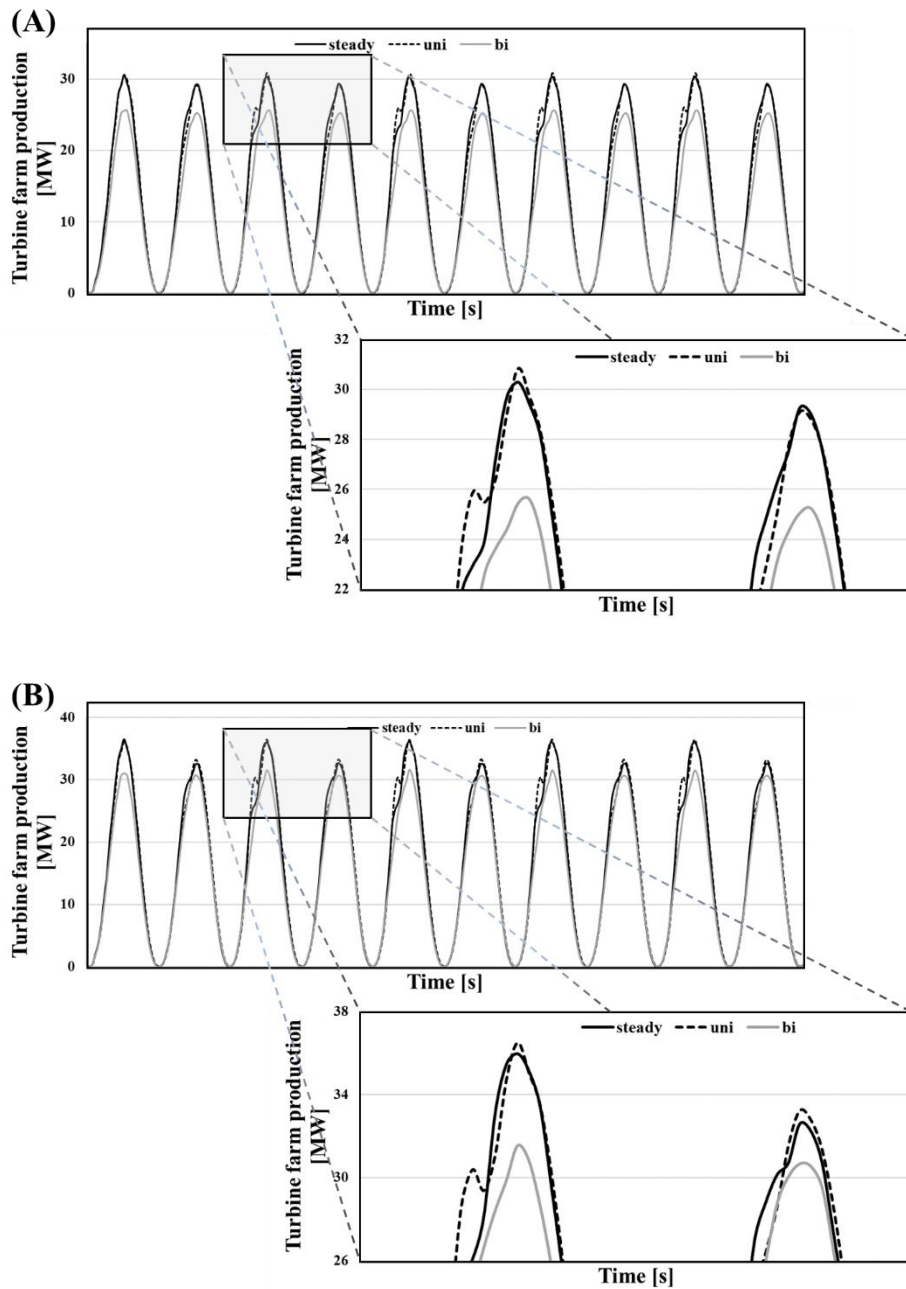


Figure 32. tidal farm production under the bidirectional flow condition for layouts optimized under different flow conditions when  $\eta_0 = 4$  m and (A)  $N = 6$  and (B)  $N = 8$

### 4.3.3 Strategy to obtain QGO for bidirectional flow condition

The optimization under bidirectional flow condition has a risk that can easily fall into the local optima. Therefore, to avoid this convergence to the local optima, it was re-optimized with the one-body layout optimized from steady condition. The turbines in this advanced optimization was found to be staggered with respect to each other in order to take advantage of local speedups between upwind turbines. The optimal layouts from this advanced optimization were found to be the most out-performing in terms of the production, hence can be assumed as a QGO for the corresponding bidirectional flow condition.

When  $\eta_0 = 4$  m and  $N = 6$ , the resulting optimized layout produces 13.55MW of energy which improves AEP by 76.9% compared to the initial regular gridded layout, 0.4% compared to the QGO found under steady flow condition over MVT, and 12.5% compared to the optimal layout initially found under bidirectional flow.

When  $\eta_0 = 4$  m and  $N = 7$ , the resulting optimized layout produces 15.19 MW of energy which improves AEP by 46.9% compared to the initial regular gridded layout, 5.4% compared to the QGO found under steady flow condition over MVT, and 1.3% compared to the optimal layout initially found under bidirectional flow.

When  $\eta_0 = 6$  m and  $N = 8$ , the resulting optimized layout produces 46.34 MW of energy which improves AEP by 40.1% compared to the initial regular gridded layout, 6.3% compared to the QGO found under steady flow condition over MVT, and 12.1% compared to the optimal layout initially found under bidirectional flow.

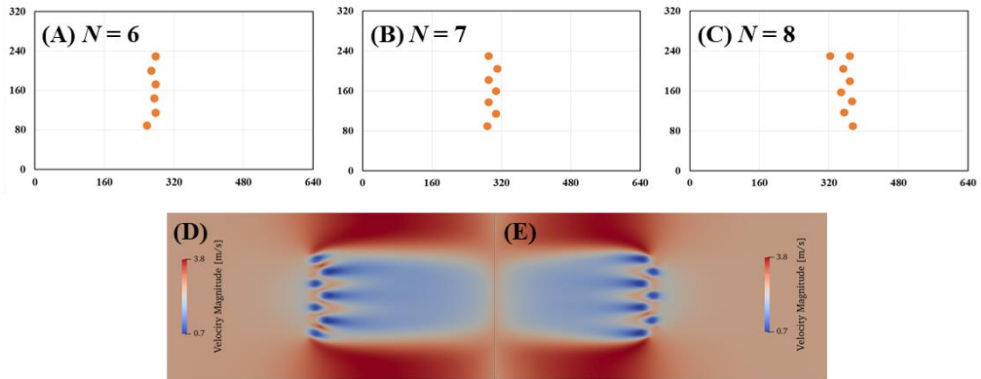


Figure 33. reoptimized layout under bidirectional flow conditions when (A)  $\eta_0 = 4$  m and  $N = 6$ , (B)  $\eta_0 = 4$  m and  $N = 7$ , (C)  $\eta_0 = 6$  m and  $N = 8$ , velocity magnitude contour for  $N = 7$  when (D) positive direction (E) negative direction

#### 4.3.4 Conclusion of Main test

- Key take-aways from optimal layouts from different flow conditions
  - Optimal layout under unidirectional flow condition is similar to the optimal layout under steady condition when it satisfies the velocity condition  $u_{max} > \frac{MVT}{0.74} \rightarrow$  This implies that the MVT to converge to QGO can be applied in the same way to the unidirectional flow.
  - Optimal layout under bidirectional conditions is totally different to the optimal layout under unidirectional conditions, to consider the wake effect from both directions. It also has a high risk to fall into local optima during the optimization procedure.
  - The performance of the optimal array for identical flow condition can vary up to 20% with optimal layouts under different flow conditions.

- Key take-aways from the strategy to obtain QGO for bidirectional flow condition
  - To avoid the risk of the optimization under bidirectional flow condition fall into local optima, it was re-optimized with the one-body layout optimized from steady condition.
  - The turbines in this advanced optimization was found to be staggered with respect to each other in order to take advantage of local speedups between upwind turbines.
  - The optimal layouts from this advanced optimization were found to be the most out-performing in terms of the production, hence can be assumed as a QGO for the corresponding bidirectional flow condition.

## CHAPTER 5. Conclusions

This study aimed to find the near-optima array configurations of tidal stream farm under unsteady flow condition in order to extract high power as possible at an idealized channel. Due to the fact that tidal flow is predictable and strongly governed by hydrodynamic governing equations, PDE-constrained gradient-based optimization was selected as optimization scheme. Governing PDE was selected as SWE with large artificial viscosity coefficient in order to assure convergence of optimization. Target functional was total generated power and turbine positions were set as controls. Channel was modeled as uniform rectangular cross-sectioned channel with constant bed friction, with the Froude number near 0.2. Since gradient-based optimization includes computing derivative of friction function during the computation process of the derivative of target functional, friction function should be continuous. Therefore, Turbine was modeled as a friction function, which was modeled as a bump function. Turbine friction coefficient  $K$  was set as 12 in order to model the wake structure similar to real turbine cases. Boundary conditions for inlet and outlet velocity was given as Dirichlet boundary condition for the steady flow and Flather boundary condition for the unsteady flow.

Before conducting main test, two pilot tests were conveyed to provide useful insight for designing main test. Throughout the pilot tests, the wake behavior under the unsteady flow and the appropriate layout comparison criteria for steady and

unsteady flow has been discovered to be applied in the main test. The appropriate comparison criteria should be based on energy production, which turns out that cyclic-averaged single turbine production under unsteady sinusoidal flow with maximum velocity of  $u_{max}$  is equal to the instant single turbine production under steady flow with approximately  $0.74 u_{max}$ . Then the heuristics of the optimal layout under steady condition were discovered together with the minimum velocity threshold (MVT) to converge to the optimal layout. The configured optimal array tends to structure one-body array: Linear fence for 5 turbines, arc-shaped fence for 6, rather sophisticated barrier for 7, M-shape layout for 8, and turbines are detached from the array when 9 turbines are deployed. The previous study illustrates the heuristics of QGO under steady condition already, however, it was found in the present study that when the flow speed is not enough to generate much wake, the optimization can lead to a different layout from QGO, which means the QGO itself is very much dependent on the flow condition.

Based on the conclusions of pilot tests, main test was conducted in order to observe the impact in optimal array configuration when the unsteady flow conditions are applied. Optimization under unsteady flow with different free-surface elevation was performed for different number of turbines, resulting in more than 120 test cases.

Optimal layout under unidirectional flow condition was found to be similar to the optimal layout under steady condition when it satisfies the velocity condition  $u_{max} > \frac{MVT}{0.74}$ . This implies that the MVT to converge to QGO can be applied in the same way to the unidirectional flow. Optimal layout under bidirectional conditions is

totally different to the optimal layout under unidirectional conditions, to consider the wake effect from both directions. It also has a high risk to fall into local optima during the optimization procedure. To avoid this convergence to the local optima, re-optimization from the one-body layout was suggested as an advanced optimization, and found to be the most out-performing in terms of the production, hence can be assumed as a QGO for bidirectional flow condition. Within this QGO, the turbines are staggered with respect to each other in order to take advantage of local speedups between upwind turbines.

This study highlights the necessity of considering the variation in flow speed and direction in the tidal turbine farm layout optimization, showing that the performance of the optimal array for identical flow condition can vary up to 20% with optimal layouts under different flow conditions. It is expected that this optimal shape of array can be implemented for array design in tidal energy resource assessment or for recommended initial condition in gradient-based optimization. Since only the simplest unsteady flow with constant amplitude and period sinusoidal forcing was considered in the present study, more advanced study can be made when considering neap-spring cycle of the tide in the future.

## REFERENCES

- [1] B. Polagye, P. Malte, M. Kawase, and D. Durran (2008). Effect of large-scale kinetic power extraction on time-dependent estuaries. *Proc. IMechE Vol. 222 Part A: J. Power and Energy*
- [2] G.Mosetti, C.Poloni, and B. Diviacco (1994). Optimization of wind turbine positioning in large windfarms by means of a genetic algorithm. *Journal of Wind Engineering and Industrial Aerodynamics 51*. 105-116.
- [3] C. Wan, J. Wang, G. Yang, and X. Zhang (2010). Optimal micro-siting of wind farms by particle swarm optimization. In: Tan Y, Shi Y, Tan K, editors. *Advances in swarm intelligence. Lecture notes in computer science*, vol. 6145. Berlin, Heidelberg, New-York: *Springer-Verlag*. 198-205.
- [4] Bilbao M, and Alba E. (2009). Simulated annealing for optimization of wind farm annual profit. In: *2nd international symposium on logistics and industrial informatics*. 1-5
- [5] Larsen, G. C., Aagaard Madsen, H., Troldborg, N., Larsen, T. J., Réthoré, P.-E., Fuglsang, P., Ott, S., Mann, J., Buhl, T., 15 Nielsen, M., and others (2011). TOPFARM-next generation design tool for optimisation of wind farm topology and operation, *Tech. Rep. Risø-R-1805(EN)*, Risø DTU National Laboratory for Sustainable Energy
- [6] S.W. Funke, P.E. Farrell, and M.D. Piggott (2014). Tidal turbine array optimisation using the adjoint approach. *Renewable Energy 63*. 658-673

- [7] M. Noel (2012). A new gradient based particle swarm optimization algorithm for accurate computation of global minimum. *Applied Soft Computing Volume 12, Issue 1, January 2012*. 353-359
- [8] J. Han, J. Jung, and J. Hwang (2021). Optimal configuration of a tidal current turbine farm in a shallow channel. *Ocean Engineering 220*. 108395
- [9] National grid Group PLC. <https://www.nationalgrid.com/stories/energy-explained/what-is-net-zero>
- [10] 환경부, 한국환경산업기술원 (2021). 한국 재생에너지 동향과 대응정책. *국내IP 환경동향보고*
- [11] Lazard (2020). Lazard's levelized cost of energy analysis – version 14.0. <https://www.lazard.com/media/451419/lazards-levelized-cost-of-energy-version-140.pdf>
- [12] H.U. Sverdrup, M.W. Johnson, and R.H. Fleming (1942). The oceans their physics, chemistry, and general biology. *New York: Prentice-Hall, Inc.* 545-564
- [13] S. Lee, H. Kwak, J. Kim, E. Lee, J. Kim, K. Jeon and Korea Water Resource Corporation (2015). The study on estimate of tidal power using Matlab T-tide Based on tide prediction. *The 52th KIEE Summer Conference 2015*
- [14] B. Simon (2013). Coastal Tides. *Institut océanographique, Fondation Albert I<sup>er</sup>, Prince de Monaco*. 22-24
- [15] J.V. Kreeke, and K. Robaczewska (1993). Tide-induced residual transport of coarse sediment; application to the EMS estuary. *Netherlands Journal of Sea Research 31 (3)*. 209-220

- [16] A. Roberts, B. Thomas, P. Sewell, Z. Khan, S. Balmain, and J. Gillman (2016). Current tidal power technologies and their suitability for applications in coastal and marine areas. *J. Ocean Eng. Mar. Energy* (2016) 2. 227–245
- [17] Marine Current Turbines ltd (2016). SeaGen-S 2MW. <https://simecatlantis.com/wp-content/uploads/2016/08/SeaGen-Brochure.pdf>
- [18] D. Byun, D. Hart, and W. Jeong (2013). Tidal current energy resources off the south and west coasts of Korea: Preliminary observation-derived estimates. *Energies* 2013, 6. 566-578
- [19] C.B. Vreugdenhil (1994). Numerical methods for shallow-water flow. *Springer Science+Business Media Dordrecht*.
- [20] R.-E. Plessix (2006). A review of the adjoint-state method for computing the gradient of a functional with geophysical applications. *Geophys. J. Int.* 167. 495–503
- [21] M.B. Giles, and N.A. Pierce (2000). An introduction to the adjoint approach to design. *Flow, Turbulence and Combustion* 65. 393–415
- [22] T. Divett, R. Vennell, and C. Stevens (2013). Optimization of multiple turbine arrays in a channel with tidally reversing flow by numerical modelling with adaptive mesh. *Phil Trans R Soc A* 371. 20120251.
- [23] R.L. Street, G.Z. Watters, and J.K. Vennard (1996). Elementary fluid mechanics. *New York: John Wiley and Sons*.
- [24] B. Kinsman (1965). Wind waves. The generation and propagation on the ocean surface. *Prentice-Halle Incorporated*.
- [25] Ryan N. King et al (2016). Adjoint Optimization of Wind Plant Layouts. *Wind*

*Energ. Sci. Discuss.* doi:10.5194/wes-2016-25

[26] Glenn S. Carter and Mark A. Merrifield (2007). Open boundary conditions for regional tidal simulations. *Ocean Modelling* 18 (2007) 194–209

## 국문초록

### 비정상유동이 조류발전단지 배치최적화에 미치는 영향

서울대학교 대학원

건설환경공학부

정원정

세계적인 기후 위기와 대기 오염으로 인해, 재생 에너지에 대한 수요가 증가하고 있다. 풍력과 태양광 발전이 신재생에너지 산업을 선도하고 있으며, 조류 발전은 높은 에너지 밀도와 예측 가능한 특성으로 인해 앞으로의 잠재력이 클 것으로 추정된다.

조류 발전은 아직 가격 경쟁의 측면에서 실용화 수준에 이르지 못했다. 가격 경쟁력을 확보하기 위한 비용절감의 수단으로는 전력 추출 극대화를 위한 노력이 필요하며, 이에 제약 조건 내에서의 터빈 배치 최적화를 위한 알고리즘에 대한 이해가 선행되어야 한다.

조류발전 단지 배치 최적화에 대한 연구는 기존에 다수 진행되어 왔으나, 비정상 유동에서의 최적화 해를 도출하는 것이 다소 복잡해 정상유동

상태의 가정이 주를 이루었다. 그러나, 조류는 달과 태양의 기조력에 의한 조류에 의해 발생하는 현상임에 따라, 비정상 유동이라는 특성이 크게 작용하는 바, 본 연구에서는 이러한 특성을 반영한 배치 최적화 연구가 진행되었다.

따라서 본 연구는 비정상 유동 하에서의 조류발전단지 배치 최적화에 관한 이해를 기반으로 이 때의 민감도 기반 최적화의 해가 전역 최적해에 수렴하는가를 수치실험을 통해 확인하는 것을 목적으로 하였다. 다양한 진폭과 방향 등의 조건에서 수백개의 수치실험이 이루어졌으며 이를 통해 비정상 유동 하에서의 조류발전단지 배치 최적화에 대한 일반적인 추세와 최적해를 확인하였다.

먼저, 정상 유동과 비정상 유동 각각에 단일 터빈을 두어 각 조건 하에서의 후류 형태와 에너지 생산량 차이를 확인하였다. 또한 정상 유동 하에서의 최적 배치 형태와 최적해에 도달할 수 있는 임계 속도 값을 도출하여 비정상 유동 하에서의 수치실험에 선행 가정으로 사용될 수 있도록 하였다. 이러한 실험 결과들을 바탕으로 비정상 유동 하에서의 조류발전단지 배치 최적화에 대한 일반적인 추세와 최적해를 확인할 수 있었다. 비정상 단방향 유동의 경우에는 임계 속도 조건을 만족하였을 때 정상 유동 하에서의 최적 배치와 비슷한 형태를 보였지만, 비정상 양방향 유동의 경우에는 터빈이 교차 배치된 형태를 최적 배치로 갖는 것을 알 수 있었다.

수치실험에는 파이썬 기반 오픈소스 소프트웨어인 OpenTidal Farm이 사용되었다. 수치실험은 직사각형 조류발전 단지 내에서 이루어졌으며, 편미분 방정식은 2차원 천수방정식을 사용했고, 목적함수는 총에너지 추출량으로 구성되었다. 또한, 터빈은 민감도 기반 최적화에 적합하게끔 범프함수로 매개변수화 되어 실험에 사용되었다.

**Keywords:** 조류발전단지 배치최적화, 비정상 유동, 민감도 기반 최적화 (Gradient-based optimization), 천수방정식, OpenTidalFarm

학번: 2019-21095